



C-AXIS ANALYSIS OF THE NEEM ICE CORE
AN APPROACH BASED ON DIGITAL IMAGE PROCESSING

JAN EICHLER

Diplomarbeit im Studienfach Physik

vorgelegt dem
Fachbereich Physik, Freie Universität Berlin

Berlin/Bremerhaven, April 2013

Die Diplomarbeit wurde am Alfred-Wegener-Institut für Polar- und Meeresforschung in der Helmholtz-Gemeinschaft in Bremerhaven unter der wiss. Betreuung von Frau Dr. Ilka Weikusat durchgeführt.

Erstgutachter: Prof. Dr. Dr. Günter Kaindl
Wiss. Betreuung: Dr. Ilka Weikusat
Zweitgutachter:

Jan Eichler: *C-Axis Analysis of the NEEM Ice Core, An Approach Based on Digital Image Processing*, © April 2013

ABSTRACT

The focus of this Diploma thesis is the development of a new approach for the analysis of crystal orientations in polar ice, based on digital image processing. The c-axes orientations are measured on thin ice sections using automated polarized light microscopy. The measured data are stored in form of high-resolution digital images which have been evaluated only manually so far. The automatic detection of grains and grain boundaries and the extraction of their orientation and shape parameters enable a statistical acquisition of the ice microstructure. The analysis of c-axes distributions, grain sizes, misorientations between adjacent grains, grain boundary orientations etc. allows for conclusions about the active recrystallization mechanisms. This is of high importance for an improved understanding of ice deformation and ice flow. The developed program is applied to analyze the microstructure in the [NEEM](#) ice core (Greenland).

ZUSAMMENFASSUNG

Diese Arbeit beschäftigt sich mit der Entwicklung einer neuen, auf digitaler Bildverarbeitung basierenden Methode zur Analyse von Kristallorientierungen in polarem Eis. Die Orientierungen der C-Achsen werden mittels automatisierter Polarisationsmikroskopie an Dünnschnittproben gemessen. Diese Messung liefert hochaufgelösten Digitalbilder, die bislang nur manuell ausgewertet wurden. Die automatische Erkennung von Körnern und Korngrenzen und die Ermittlung von deren Orientierungs- und Geometrieparametern bieten die Möglichkeit, die Mikrostruktur im Eis statistisch zu erfassen. Die Analyse der C-Achsen-Verteilungen, Korngrößen, Misorientierungen zwischen Nachbarkörnern, Korngrenzrichtungen etc. erlaubt es, Rückschlüsse auf die wirkenden Rekristallisationsmechanismen zu ziehen. Letzteres ist von großer Bedeutung für ein besseres Verständnis von Eisdeformation und Eisfließverhalten. Das entwickelte Programm wird angewandt um die Mikrostruktur im [NEEM](#) Eisbohrkern (Grönland) zu analysieren.

CONTENTS

1	INTRODUCTION	1
2	THEORETICAL BACKGROUND	3
2.1	Ice Crystal Structure	3
2.2	Polycrystalline Ice	4
2.3	Ice Creep	5
2.4	Recrystallization	7
2.5	Glen's Flow Law	9
3	EXPERIMENTAL TECHNIQUE	11
3.1	Laboratory Work	11
3.2	C-Axes Orientation Measurements	12
3.2.1	Birefringence	12
3.2.2	Polarized-Light Microscopy	14
3.2.3	Automatic Fabric Measurements	16
4	IMAGE ANALYSIS OF FABRIC DATA	19
4.1	Fabric Image	19
4.1.1	Metric	19
4.1.2	Error Estimation	21
4.1.3	Color Code	23
4.2	Preprocessing Routines	24
4.2.1	Noise Reduction	24
4.2.2	Tile Shift	25
4.3	Main Routine: Grain Network Detection	26
4.3.1	Image Segmentation	26
4.3.2	Extraction of Parameters	30
4.3.3	Segmentation Errors	31
4.4	Program Execution	32
5	RESULTS: APPLICATION TO THE NEEM ICE CORE	35
5.1	The NEEM Ice Core	35
5.2	Classical Analysis: Anisotropy	36
5.2.1	Preliminaries	36
5.2.2	Variation over the Whole Core Length	38
5.2.3	High Resolution Studies	41
5.3	Misorientation between Adjacent Grains	42
5.4	Grain Boundary Geometry	46
5.4.1	Low Angle Boundaries: N-Type vs. P-Type	49
5.4.2	Deviation from the Symmetric Tilt Boundary	50
6	SUMMARY AND OUTLOOK	55
A	APPENDIX	57
	BIBLIOGRAPHY	59
	ACKNOWLEDGMENTS	63

LIST OF FIGURES

Figure 1	Ice I _h crystal structure	3
Figure 2	Firn and ice	5
Figure 3	Dislocations	6
Figure 4	Creep curve	7
Figure 5	Rotation recrystallization	8
Figure 6	Laboratory tools	11
Figure 7	Polarization microscopy	15
Figure 8	G50 Fabric Analyser	17
Figure 9	Inclination image	20
Figure 10	Error estimation	22
Figure 11	Equal-area projection	23
Figure 12	Orientation color code	24
Figure 13	Median filter	25
Figure 14	Tile rotation	26
Figure 15	Mean misorientation	28
Figure 16	Grain detection	29
Figure 17	Artificial grain boundaries	31
Figure 18	cAxes program execution	33
Figure 19	NEEM ice core location	35
Figure 20	Woodcock parameter	38
Figure 21	NEEM ice core profile	39
Figure 22	Grain size & Woodcock parameter	40
Figure 23	Running mean	42
Figure 24	Eigenvalue grain size correlation	43
Figure 25	Adjacent grains misorientation	44
Figure 26	Random pair misorientation	45
Figure 27	Adjacent vs. random pairs	46
Figure 28	Fraction of linear grain boundaries	47
Figure 29	Grain boundary orientations	48
Figure 30	N-type vs. P-type grain boundary	50
Figure 31	Symmetric Tilt Boundary	51
Figure 32	Deviation from basal tilt boundary	52
Figure 33	Orthogonal planes	53
Figure 34	Intragranular structures	56

LIST OF TABLES

Table 1	Refractive indices	13
Table 2	Error estimation	23
Table 3	Program input parameters	33

ACRONYMS

AWI	Alfred-Wegener-Institut Helmholtz-Zentrum für Polar- und Meeresforschung
DIP	Digital Image Processing
EBSD	Electron Backscatter Diffraction
GB	Grain Boundary
LASM	Large Area Scan Macroscope
LGGE	Laboratoire de Glaciologie et Géophysique de l'Environnement
NEEM	North Greenland Eemian Ice Drilling
PDF	Probability Density Function

INTRODUCTION

The frozen part of the Earth's surface is referred to as the cryosphere. It forms an integral part of the global climate system with all its complexity of interactions, dependencies and feedbacks between the sub-systems studied by the respective climate sciences. Glaciology is an interdisciplinary science which studies diverse phenomena occurring in glacial ice. *Glaciers* are ice masses usually formed within a mountain relief due to snow compaction. There are more than 160,000 glaciers spread all over the world's continents. Larger glacial ice masses are referred to as *ice caps* and ice bodies of continental size are called *ice sheets*. The only two present-day ice sheets on Earth are the Antarctic Ice Sheet and the Greenland Ice Sheet, both featuring a thickness of more than three kilometers. The following table shows the area, ice volume and the sea-level rise equivalent of the two ice sheets compared to the rest of the glacial ice stored in glaciers and ice caps (Church et al., 2001).

	Antarctic ice sheet	Greenland ice sheet	Glaciers and ice caps
Area (10^6 km^2)	12.37	1.71	0.68
Volume (10^6 km^3)	25.71	2.85	0.18
Sea-level rise equivalent (m)	61.1	7.2	0.50

Large ice bodies are highly dynamic systems. Gravity-induced ice deformation leads to a viscoplastic flow of the material from elevated regions down to the valleys and coasts. The fastest glaciers race down the valley at surface velocities reaching several tens of meters per day. In order to study ice-sheet dynamics and to predict future changes, numerical ice flow models have been developed, incorporating a high variety of complex boundary conditions (e.g. the bed-rock interaction, temperature gradient, melt-water hydrology etc.). Nevertheless, a limiting factor is the still insufficient understanding of the internal processes responsible for the deformation of ice.

From the geological point of view, ice sheets and glaciers are in fact rocks (rather than fluids) naturally deforming due to solid-state deformation mechanisms including strain-induced recrystallization. The characteristic features of ice as a mineral are the very low impurity concentration and the temperature very close to the melting point.

Since 1964, when the first ice core was drilled through an ice sheet at the Camp Century base in Greenland, ice-core physics has differ-

entiated into a wide range of analytical techniques focusing on different problems and questions. Probably the most commonly known challenge of the ice-core studies might be the reconstruction of paleoclimatic records up to several hundreds of thousands of years into the past. On the other hand – and here I come to the topic of this Diploma thesis – ice-core drilling also provides a unique insight into the crystal structure of the deforming material. An ice core samples an ongoing natural experiment over thousands of years.

The topic of this Diploma thesis is the analysis of ice crystal orientations obtained by polarized light microscopy of thin sections. This experimental technique makes use of the optical anisotropy of ice to determine the spatial orientation of the main symmetry axis of the hexagonal lattice – the c-axis. Due to the development of automated and compact polarized-light microscopes (fabric analyzers) in recent years c-axis fabric images of high resolution became available. The amount and quality of the measured data call for the application of new analysis methods. Thus, the goal of this thesis is to investigate the potential of Digital Image Processing (DIP) applied to the c-axes orientation data. This is put into practise by developing a computer program with the purpose to automatically detect microstructural features such as individual crystals and boundaries between them. It is assumed that an appropriate analysis of their shapes and orientations can lead to a better understanding of the active recrystallization processes.

The content of the thesis is organized as follows: [Chapter 2](#) provides the theoretical background describing the crystal structure of natural ice and introducing processes that are responsible for the plastic deformation. [Chapter 3](#) treats the measuring method giving a brief introduction of birefringence and the concepts of polarized light microscopy. [Chapter 4](#) describes the functionality of the developed program for image analysis of the c-axes orientation data. The program was applied to process data measured on the [NEEM](#) ice core. The results are presented and discussed in [Chapter 5](#). At the end, a brief summary of the results of this thesis is given.

THEORETICAL BACKGROUND

This chapter gives an overview of the relevant properties of ice. Important terms, such as *basal plane*, *c-axis*, *dislocation* and *creep* are introduced. The first two sections treat the structures of both monocrystalline and polycrystalline ice, the latter appearing in ice sheets and glaciers. Crystal defects and deformation related processes are described in the following sections. Lastly, the flow law currently used in ice sheet modeling is introduced.

2.1 ICE CRYSTAL STRUCTURE

The water molecule consists of one oxygen and two hydrogen atoms. It contains ten electrons: two of them in the 1s shell around the oxygen nucleus and the remaining eight in pairs occupying four sp hybrid orbitals. Two of these orbitals participate in the two O – H bonds, the other two are lone-pair orbitals. In a free molecule, the distance between the oxygen and hydrogen nuclei is $0.9572 \pm 0.0003 \text{ \AA}$ and the angle between the two covalent bonds is $104.52 \pm 0.05^\circ$ (Petrenko and Whitworth, 1999).

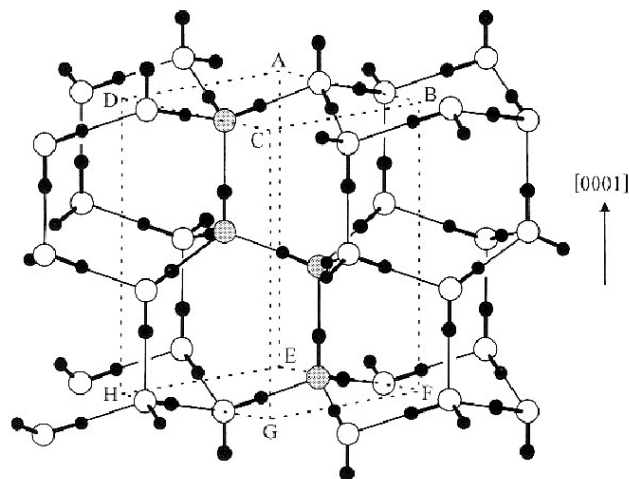


Figure 1: Ice I_h crystal structure from Petrenko and Whitworth (1999) with oxygen atoms (white) and hydrogen atoms (black). The thick short lines represent covalent bonds, long thin lines are hydrogen bonds. The eight points ABCDEFGH mark the unit cell, which contains four oxygens (shaded).

The non-linearity of the H₂O molecule and the high electronegativity of oxygen are sources of many important features of water, primarily its polar nature and its ability to build hydrogen bonds.

Although the existence of 12 solid phases of water has been demonstrated so far, hexagonal ice (I_h) is the only stable form under natural pressure and temperature conditions. The crystal structure of I_h is shown in [Figure 1](#). Each oxygen atom is surrounded by four oxygen atoms that form a regular tetrahedron. The hydrogens are covalently bonded to their nearest oxygens on one side and participate in a hydrogen bond linking another oxygen on the other side. This alignment gives rise to a hexagonal ZnS-type crystal structure. The dimensions of the unit cell at -20°C , obtained through X-ray diffraction, are: $a = 4.5169 \text{ \AA}$ and $c = 7.3570 \text{ \AA}$ ([Hobbs, 1974](#)). The molecules are concentrated in a series of planes parallel to the (0001) plane. These are called basal planes and the symmetry axis normal to them is referred to as the *c-axis*. The present thesis revolves - so to speak - around the *c-axis*.

2.2 POLYCRYSTALLINE ICE

Ice in ice sheets and glaciers is a product of *firn* compaction. During new snow accumulation, older snow layers experience a pressure increase. Initially separated snow grains get connected through a process analog to sintering in ceramics. This compact, porous, air permeable snow is referred to as *firn* ([Figure 2a](#)).

With increasing depth, bonds between grains become stronger and the density increases. When the density reaches about 830 kg/m^3 , air channels close off forming air bubbles (see example [Figure 2b](#)). This zone is called *firn-ice transition* and its depth depends mostly on the precipitation rate and temperature.

Further densification results from the compression of air bubbles by creep of the material. When the air pressure exceeds the dissociation limit, bubbles disappear and the air molecules are stored within a *clathrate hydrate* crystal structure. The disappearance of air bubbles takes place typically from 800 to 1000 meters depth ([Paterson, 1994](#)).

Due to its origin, glacier ice is not formed by a single crystal, but rather consists of a large number of crystallites, also called *grains*. Grain size, shape (texture) and lattice orientation (fabric¹) exhibit strong spatial and temporal variation. The typical grain size varies from tenths of millimeters up to several centimeters in diameter.

The interface between two adjacent grains is called the *Grain Boundary* (*GB*). It is a planar lattice defect – the molecules on *GBs* do not follow the crystal alignment rules. The molecular structure of ice grain boundaries is not well understood so far.

¹ No terminology convention exists for the use of *texture*, *fabric* and *microstructure*. In materials science or geology these expressions may refer to different features.

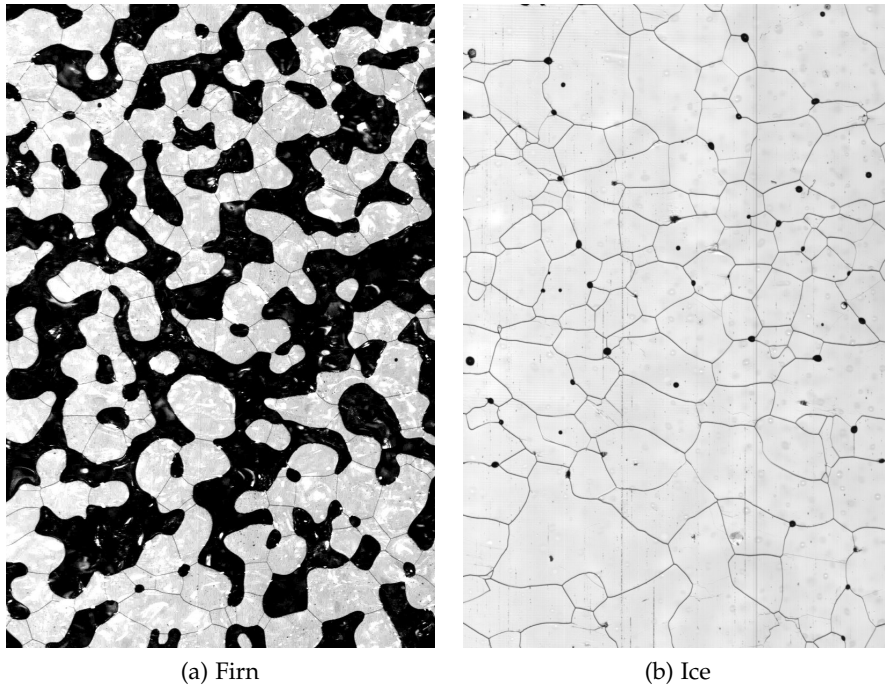


Figure 2: (a) Surface of a section through a firn sample from 11 m depth, B36 ice core, Antarctica, image courtesy of Johannes Freitag.² The air-filled space between the crystallites appears dark. Boundaries between individual grains can be observed as thin black lines. (b) Ice from 273 m depth, NEEM ice core, Greenland, image courtesy of Tobias Binder.³ The air volume is reduced to a number of small bubbles. Both sections were recorded by the Large Area Scan Macroscope (LASM).

2.3 ICE CREEP

Creep is a plastic deformation of a solid body under the influence of stress. In this context the solid exhibits characteristics of a viscous fluid. Large ice bodies such as ice sheets and glaciers deform under their own weight. This leads to the plastic flow of the ice masses from higher regions down to the valleys and coasts. On large time scales, single ice crystals deform even under the application of very low stress. The ease with which the ice creep can be activated is explained through the movement of *dislocations* through the crystal lattice.

Dislocations are crystallographic defects which introduce additional half-planes into the crystal and thus produce linear lattice discontinuities - the dislocation lines (Figure 3). They are responsible for important mechanical properties of crystalline materials, such as plasticity of metals and creep of ice. In dislocation theory, the character of dis-

² Alfred-Wegener-Institut Helmholtz-Zentrum für Polar- und Meeresforschung (AWI)

³ Interdisciplinary Center for Scientific Computing (IWR), Ruprecht-Karls-University of Heidelberg

locations is described by the *Burgers vector* (Weertman and Weertman, 1992). Consider a closed path through the crystal lattice, which starts and ends at the same position. In a square-shaped two-dimensional lattice this would be realized through a path consisting of the same number of steps to the right as to the left, and the same number of steps up and down. If the circuit includes a dislocation it will no longer start and end at the same position. The Burgers vector is defined to be this closure failure - it is the vector between the end point and the start point of the circuit.

There are two elementary dislocation types - the *edge* and the *screw* dislocations (Figure 3). The Burgers vector of an edge dislocation is perpendicular to the dislocation line. On the other hand, in a screw dislocation, the Burgers vector and the dislocation line are parallel to each other. More complex dislocations exist as combinations of these two types.

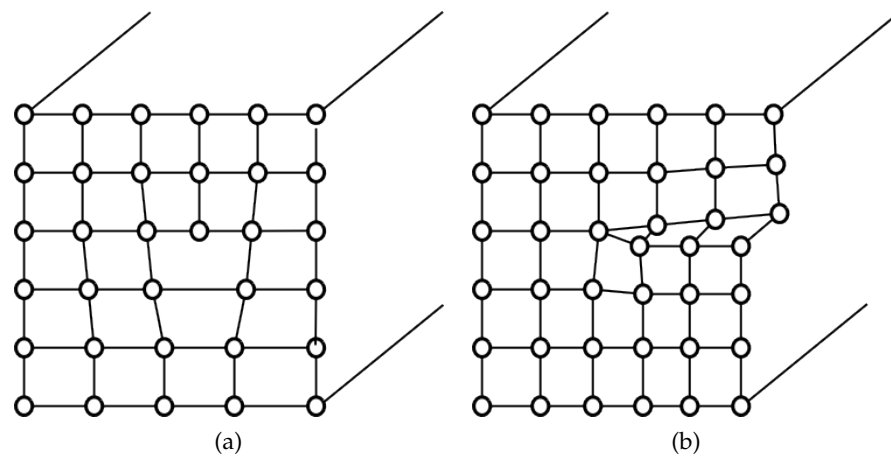


Figure 3: (a) Edge and (b) screw dislocation, for the simplicity a simple cubic lattice was drawn.

Dislocations can easily move through the lattice. Such a migration of the defects produces a slip of two parts of the lattice against each other and leads to crystal deformation. The dislocation creep in ice occurs predominantly along the basal slip system. Although non-basal slip systems exist,⁴ for their activation much higher stresses are required than for the basal slip. This makes single ice crystal to one of the mechanically most anisotropic natural materials.

Creep of Polycrystalline Ice

A most famous and currently applied study on deformation of polycrystalline ice was described by Glen (1955). An aggregate formed by a number of differently oriented grains cannot deform in a mutually

⁴ prismatic $(10\bar{1}0)$, pyramidal $(10\bar{1}1)$

compatible way due to the high mechanical anisotropy of each individual grain. Crystals that are favorably oriented for the basal slip will start to deform first. However, their deformation is blocked by their neighbors. This leads to internal stresses that play an important role in further deformation.

Jacka and Jun (2000) carried out a number of deformation experiments on laboratory-prepared polycrystalline samples with random grain orientations. Figure 4 shows a typical creep curve for polycrystalline ice under constant stress. The immediate strain after application of stress (AB) is caused by the elastic reaction of the material. This is followed by a decelerating plastic deformation (BC) called *primary creep*. This creep is related to the deformation of the individual grains due to dislocation glide (as described above). The internal stresses produced by this processes slow down the deformation until a minimal strain rate is achieved (around C). This state is called *secondary creep*. After some time the deformation accelerates again reaching a new steady state of maximal strain rate - the *tertiary creep* (DE). This final steady state is hard to attain in laboratory experiments due to the very long time scales. Nevertheless, it is very important for the natural ice flow studies, since tertiary creep is associated with *dynamic recrystallization* (see next section).

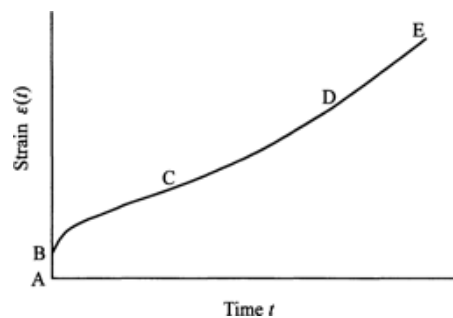


Figure 4: Creep curve of polycrystalline ice, taken from Petrenko and Whitworth (1999). AB: elastic deformation of the aggregate; BC: primary creep; C: secondary creep; CD: deformation acceleration due to dynamic recrystallization; DE: final steady state (tertiary creep).

2.4 RECRYSTALLIZATION

Large polycrystalline bodies, e. g. rocks and glaciers, store a large amount of energy in crystal defects such as grain boundaries and dislocations. Recrystallization mechanisms driven by the reduction of stored energy are present in all depths of ice sheets. If recrystallization takes place during deformation, it is referred to as dynamic recrystallization. Drury and Urai (1990) distinguish between two basic types of dynamic processes which are called *rotation recrystallization*

and *grain boundary migration*. Static processes such as the *normal grain growth* are not related to the ice flow.

Normal Grain Growth

Normal grain growth is observed in the first few hundred meters below the surface. It is characterized by the linear increase of grain area with time. The driving force of this process is the reduction of interfacial free energy of grain boundaries, which is achieved by reducing their curvature and total area. This process is similar to the growth of air bubbles in a foam. The stop of the grain growth observed in ice sheets typically a few hundred meters below the surface is explained in the classical view through the initiation of *rotation recrystallization*. Some recent studies as well as the results presented in [Section 5.3](#) call this point into question.

Rotation Recrystallization

Rotation recrystallization (also polygonization) refers to a process in which old grains are subdivided into a number of new smaller grains. This occurs when heterogeneous local stresses act on a grain in a way that it gets bent. If the orientation is favorable for dislocation glide, dislocations align into an array forming a discontinuity in the crystal orientation - i. e. a new low-angle boundary. By progressive rotation of the two subgrains, the misorientation angle increases so that finally a regular high angle boundary develops between the grains ([Figure 5](#)).

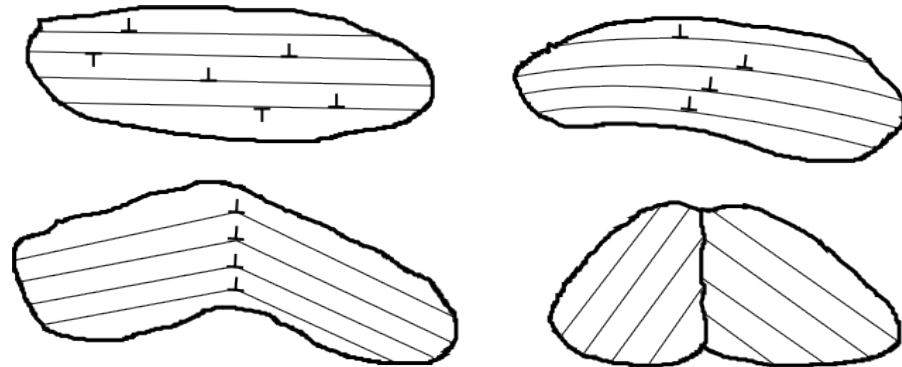


Figure 5: Rotation recrystallization illustrated in four steps. The lines represent the basal planes. At the beginning, the crystal contains all types of dislocations. Through bending dislocations of one type align forming a new grain boundary.

Migration Recrystallization

Concerning metals the capability of grain boundaries to move has been known for a long time. The mobility of the boundaries is a function of various factors, in particular crystal structure, temperature, pressure and impurity content. Many experimental studies have shown that the migration activation enthalpy is higher for low-angle boundaries than for random high-angle boundaries (Gottstein and Shvindlerman, 1999).

The driving force of strain induced migration recrystallization in ice is the reduction of lattice energy stored in dislocations, point defects and subgrain boundaries. Grain boundaries tend to move towards regions with high dislocation density, leaving behind recovered crystals with low density of crystallographic defects.

2.5 GLEN'S FLOW LAW

Based on laboratory shear experiments, Glen (1955) proposed to describe polycrystalline ice as a non-linearly viscous fluid. The following relationship is called *Glen's flow law*:

$$\dot{\gamma} = A\tau^n \quad (1)$$

with

$\dot{\gamma}$ strain rate

A fluidity, depending on temperature, impurity content, etc.

τ shear stress

n stress exponent

It should be mentioned that Glen's flow law is an empirical fit based on the secondary creep experiments at stresses 10^2 to 10^3 times higher than those in nature. It does not consider any relevant micro-processes, such as the dynamic recrystallization discussed above. Thus, a current challenge in glaciology is to introduce a flow law taking into account the full range of physical processes as they occur under natural condition in ice sheets.

EXPERIMENTAL TECHNIQUE

This chapter covers the experimental part of the thesis, i. e. the methodical and theoretical background of the ice *c-axis* orientation measurements using *polarized light microscopy*. This method makes use of the *birefringence* of linearly polarized light in optically anisotropic materials such as ice. An automated device is used for the *c-axes* orientation records, which creates high resolution fabric images.

3.1 LABORATORY WORK

For the crystal orientation measurements, thin sections of ice have to be fabricated. Typical sizes are $100 \times 70 \times 0.3$ mm. The sample preparation is a time-consuming manual process, which has to be done either directly in the field or in the ice laboratory. Strong decrease in hydrostatic pressure and temperature changes after exhumation of the ice core from the borehole to the surface lead to material relaxation. In order to reduce these effects, immediate sample preparation and measurements in the field are more preferable. For experimental work “at home”, the [AWI](#) in Bremerhaven has a number of ice laboratories with controlled temperature conditions at its disposal.

The basic instrument for the preparation of thin ice sections are a band saw for raw cuts and a microtome. The microtome is a tool originally developed for the preparation of biological samples and medical thin sections. It consists of a very sharp blade and a mobile stage. A micrometer screw is used for precise adjustment of the distance between the stage and the blade. This assembly allows to cut

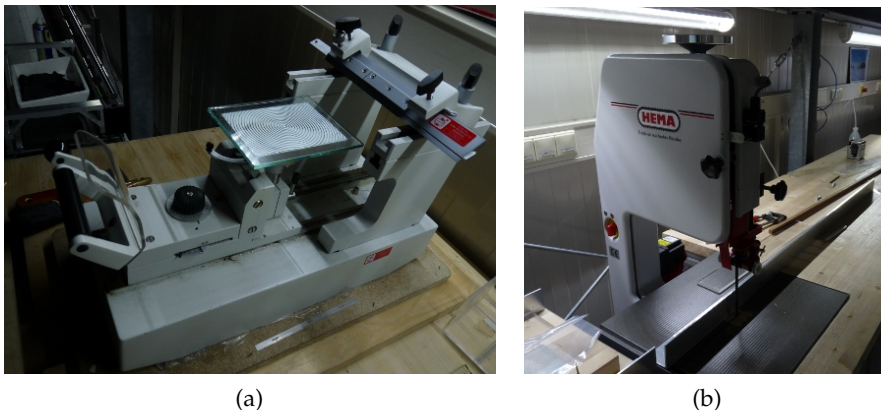


Figure 6: (a) microtome and (b) band saw for the preparation of thin ice sections in the ice laboratory at [AWI](#).

extremely thin slices of material. Both, the band saw and the microtome are operated manually. Therefore adequate precautions have to be taken.

The fabrication of a thin ice section can be summarized in the following steps:

1. Cutting of a piece of the desired surface area size.
2. Burnishing of the surface with a microtome and sublimation.
3. Face-to-face positioning of the sample on a glass holder, fixing with a thin water film.
4. Cutting of the opposite side.
5. Microtoming the thin section until the optimal thickness is reached (300 μm), polishing the surface by tiny microtome steps.
6. Surface sublimation.

3.2 C-AXES ORIENTATION MEASUREMENTS

The orientation of the c-axes is measured using polarized light microscopy. This method makes use of the birefringence of polarized light in optical anisotropic media. Unlike other methods, like Electron Backscatter Diffraction (EBSD) or X-ray Laue Diffraction, this technique does not allow to measure the full crystal orientation – in particular the a-axis orientation of the ice crystals cannot be determined. However, the c-axis being the axis of mechanical anisotropy is of major interest in deformation studies. The information loss, though regrettable, is outweighed by a number of advantages connected to the simplicity of the method. Among them a better applicability in the field due to the high mobility of the devices. Moreover, this method - in combination with automatic fabric analyzers that have been available for a couple of years by now - allows for the collection of large amounts of data which are the prerequisite for reliable statistical analysis.

3.2.1 Birefringence

In dielectrics, the polarization field \mathbf{P} induced by an electric field \mathbf{E} is given by

$$\mathbf{P} = \epsilon_0 \chi \mathbf{E}, \quad (2)$$

where ϵ_0 is the vacuum permittivity and χ the electric susceptibility of the material, which is related to the refractive index n by

$$n = \sqrt{1 + \chi}. \quad (3)$$

Wavelength λ (nm)	n_o	n_e
405	1.3185	1.3200
436	1.3161	1.3176
492	1.3128	1.3143
546	1.3105	1.3119
589	1.3091	1.3105
624	1.3082	1.3096
691	1.3067	1.3081

Table 1: Refractive indices of ice taken from [Petrenko and Whitworth \(1999\)](#).

In optically isotropic media, such as glass, air, etc., χ is a scalar quantity and \mathbf{P} is parallel and proportional to \mathbf{E} . On the other hand, in optically anisotropic media, such as crystals, χ and consequently also n are second order tensors, i. e. ,

$$\chi = \begin{pmatrix} \chi_{xx} & \chi_{xy} & \chi_{xz} \\ \chi_{yx} & \chi_{yy} & \chi_{yz} \\ \chi_{zx} & \chi_{zy} & \chi_{zz} \end{pmatrix}. \quad (4)$$

Both, the orientation and the magnitude of \mathbf{P} do not only depend on \mathbf{E} , but also on the crystal geometry. Light propagating through a crystal is refracted according to different refraction indices depending on its polarization and propagation direction within the crystal. This phenomenon is called *birefringence*.

Choosing the appropriate coordinate system, the tensor χ can be written in diagonal form:

$$\chi_{ij} = 0 \text{ for } i \neq j. \quad (5)$$

The particular case $\chi_{xx} = \chi_{yy} \neq \chi_{zz}$ is that of uniaxial anisotropy, and the z -direction is known as the optical axis of a crystal. Light traveling through an uniaxial crystal polarized at a random angle to the optical axis decomposes in two components:

- an ordinary component, with \mathbf{E} oscillating perpendicular to optical axis (z -direction), refraction index $n_o = \sqrt{1 + \chi_{zz}}$ and phase speed $v_o = c/n_o$;
- an extraordinary component, with \mathbf{E} oscillating parallel to optical axis, refraction index $n_e = \sqrt{1 + \chi_{xx}} = \sqrt{1 + \chi_{yy}}$ and speed $v_e = c/n_e$.

Materials with $n_e > n_o$ (i. e. the extraordinary ray is faster than the ordinary) are called positive.

Ice with its hexagonal lattice structure is uniaxial positive, with the c -axis being the optical axis of the crystal. [Table 1](#) shows refractive

indices of ice in the visible region for ordinary (n_o) and extraordinary (n_e) waves.

3.2.2 Polarized-Light Microscopy

In this section the principles of polarized-light microscopy are described. The following experimental setting is considered (see [Figure 7](#)): Two polarization filters – the polarizer (p) and the analyzer (a) – are situated parallel to each other in the x-y plane with polarization directions perpendicular to each other ($\varphi_a - \varphi_p = 90^\circ$). Monochromatic light (wavelength λ), emitted by a source placed below the crossed polaroids expands in z-direction, passes through the polarizer as well as through the analyzer, and is absorbed by a CCD camera to measure its intensity. If no sample is placed between the polaroids, the light polarized by the polarizer will be fully absorbed by the analyzer and will not arrive at the camera.

Now, a thin section of ice (thickness d) is placed between the polaroids. The c-axis can be represented by a unit vector, in spherical coordinates:

$$\mathbf{c} = \begin{pmatrix} \sin \theta \cos \varphi \\ \sin \theta \sin \varphi \\ \cos \theta \end{pmatrix} \quad (6)$$

Its orientation is given by the azimuth φ and the inclination θ . The angle between the polarizer's polarization direction and the c-axis projection into the x-y plane is $\beta = \varphi_p - \varphi$. Linearly polarized light of intensity A_p splits in the crystal into the ordinary and extraordinary components, with amplitudes

$$A_o = A_p \cos \beta \quad (7)$$

$$A_e = A_p \sin \beta. \quad (8)$$

Because of different refraction indices, the two waves attain a phase difference. After passing through the sample of thickness d , the phase difference will be

$$\Delta = \frac{2\pi d}{\lambda} (n_e - n_o). \quad (9)$$

At the second polarization filter, only the components parallel to the polarization direction of the analyzer can pass (i. e. at right angle to the first polarizer):

$$A_{oa} = A_o \sin \beta \quad (10)$$

$$A_{ea} = A_e \cos \beta. \quad (11)$$

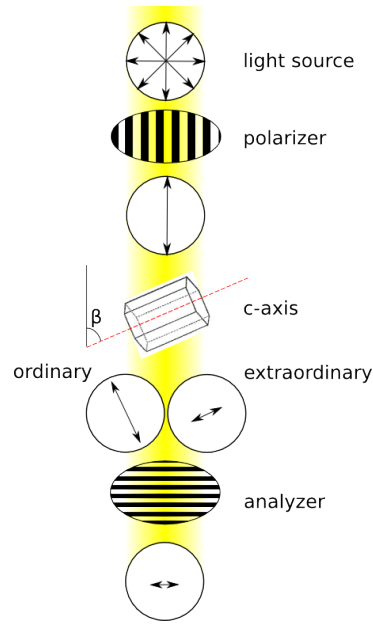


Figure 7: Linearly polarized light decomposes in the crystal into the ordinary and the extraordinary wave. After passing through the analyzer, the two components interfere and the resulting intensity is measured.

After passing through the analyzer, the ordinary and the extraordinary beams will interfere, with the resulting intensity being given by:

$$\begin{aligned} A^2 &= A_{oa}^2 + A_{ea}^2 + 2A_{oa}A_{ea} \cos \Delta \\ &= A_p^2 \sin^2 2\beta \left(1 + \cos \frac{2\pi d}{\lambda} (n_e - n_o) \right). \end{aligned} \quad (12)$$

Equation 12 is an expression for the brightness of a point recorded by the camera as a function of β . The four cases $\beta = 0, \frac{\pi}{2}, \pi,$ and $\frac{3}{2}\pi$, when A equals zero, are called extinction positions. Extinction can be achieved through rotation of the polarization filters with respect to the crystal until the c-axis stays parallel or perpendicular to the light vibration direction. The four extinction angles are thus the four candidates for the c-axis azimuth.

In order to determine the inclination θ , the measurement has to be repeated under a different view angle. This can be realized by changing the orientation of the sample on a universal stage, or changing the camera and/or the light source position. The general rotation of the coordinate system around the z and x axis is given by

$$R_{zx}(\phi, \vartheta) = \begin{pmatrix} \cos \phi & \sin \phi & 0 \\ -\sin \phi \cos \vartheta & \cos \phi \cos \vartheta & \sin \vartheta \\ \sin \phi \sin \vartheta & -\cos \phi \sin \vartheta & \cos \vartheta \end{pmatrix}. \quad (13)$$

The c-axis vector can then be written in the rotated system coordinates φ', θ' : This can be realized by rotating the crystal on a universal

stage or changing the camera position. Applying this transformation on the c-axis vector provides a system of three equations:

$$\begin{pmatrix} \sin \theta' \cos \varphi' \\ \sin \theta' \sin \varphi' \\ \cos \theta' \end{pmatrix} = R_{zx}(\phi, \vartheta) \begin{pmatrix} \sin \theta \cos \varphi \\ \sin \theta \sin \varphi \\ \cos \theta \end{pmatrix}, \quad (14)$$

where ϑ and ϕ are the rotation angles controlled by the experimenter, φ and φ' can be determined through extinction (four candidates for each), and θ and θ' are the two unknowns. The solution of this system of equations provides therefore four candidates for the inclination θ .

Repeating this procedure with a different rotation of the coordinate system, another set of four inclination candidates will result. Among these eight possible values of θ , two are the same (Wang, 1999). This angle is the true inclination angle, and the corresponding extinction angle is the true azimuth of the measured c-axis.

3.2.3 Automatic Fabric Measurements

Traditionally, the determination of the extinction angles described above was executed manually for each single point by rotating the sample on a universal stage. The measurement of one thin section was thus very time-consuming, allowing only a limited number of measured c-axes. The possibilities of fabric analysis were improved to a great extent due to the development of automated polarized-light microscopes (fabric analyzers) in the last ten years. The first automated c-axis-fabric analyzers became available around 2000 (Wang, 1999). However, these devices provided automated determination of the c-axis orientations without any automated analysis of the data. Individual points within the data matrix had to be picked manually. Improved fabric analyzers provided the c-axis orientations within a section coded as digital images (Wilson et al., 2003). During the last years faster computers permitted a faster analysis and a higher optical resolution. This allows to study the variability of the c-axis distributions within a single section on the grain- or centimeter-scale on one hand as well as on the meter-scale on the other hand, if an adequate analysis method is available.

This section will briefly introduce the *G50 Fabric Analyser* as described by Wilson et al. (2003), which is currently used at the AWI. G50 is the fifth series of automatic devices for c-axis measurements developed by Russel-Head Instruments. The light source consists of nine LEDs – one vertical and eight inclined – arranged in a circle around the vertical axis. The crossed polarizers are rotated by a motor in eight steps from 0° to 90° . The transmitted light is recorded by a CCD camera located above an objective lens. The field of view of the camera is a 10×10 mm square, and the maximal resolution is $5 \mu\text{m}/\text{pixel}$. An x-y motorized stage moves the thin section below the

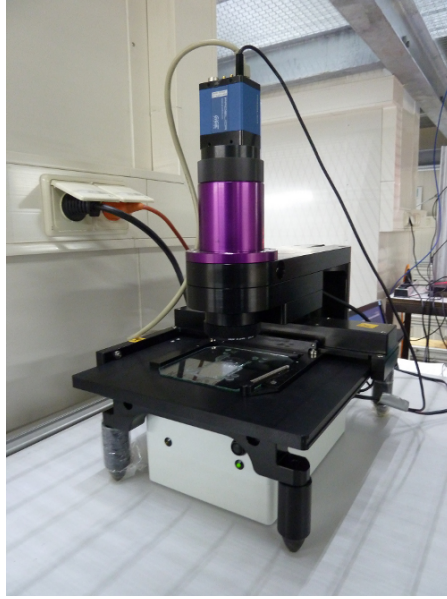


Figure 8: The G50 Fabric Analyser, photo by Anneke Tammen

objective so that at the end a complete fabric image of the whole sample can be recomposed from the individual 10×10 mm records. The maximal length of a thin section is 10 cm. Upon selecting the area and the resolution, the measurement is fully automatic, operated by a computer. The acquisition time for 1000×1000 output pixels is approximately 4 minutes.

The output is a binary file containing a raster of a given resolution, where each point carries the following data:

- Azimuth angle of the c-axis vector $0^\circ \leq \varphi < 360^\circ$;
- Inclination from the vertical axis $0^\circ \leq \theta < 90^\circ$;
- Geometrical quality $0 \leq gq \leq 100$;
- Retardation quality $0 \leq rq \leq 100$.

φ and θ are the spherical coordinates of the c-axis vector, gq and rq estimate the confidence of the measured orientations. A typical measurement of a 7×10 cm thin section, with a resolution of $20 \mu\text{m}/\text{pixel}$, takes approximately one hour, resulting in a raster image with a size of 3500×5000 pixel = 17.5 Mpix.

Since fabric records of such high resolution became available only recently, new data processing techniques have to be developed (Durand et al., 2006). The *Investigator* software package provided with the G50 device allows only picking of individual points in the c-axes image manually or using a regular grid. An adequate data analysis is required to benefit from the full information contained in the fabric images. Digital-image analysis methods are well suited for this purpose.

The main goal of this thesis was to apply techniques based on Digital Image Processing (DIP) to the analysis of the high resolution *c*-axis orientation images. To this purpose, I started the development of *cAxes* – a program written in C++ making use of the `VIGRA` library and the `CGP` package, both developed at the Heidelberg Collaboratory for Image Processing (HCI), University of Heidelberg.

DIP techniques enable advanced analysis approaches such as the topology extraction and image segmentation. In this way grains and grain boundaries can be detected automatically by the program and their shapes and orientation parameters can be evaluated. This chapter describes the functionality of the program. First, relevant characteristics of *c*-axis fabric images are introduced followed by the preprocessing routines (Section 4.2). The main routine including the detection of grains and grain boundaries is described in Section 4.3.

4.1 FABRIC IMAGE

As mentioned in Section 3.2.3, the fabric records are 2D matrices, where each point is assigned the azimuth and the inclination (the spherical coordinates) of the corresponding *c*-axis vector as well as the quality parameters of the measurement.

Figure 9 shows a gray-scale-coded inclination record produced by the G50. The image consists of a number of areas with different *c*-axis inclinations – the grains. The boundaries between individual grains exhibit a finite thickness of several pixels (see detail). This is not the real thickness of the grain boundary, but rather a volume effect of the thin section. The more inclined the interface between two grains is with respect to the image plane, the more area (or width) will it exhibit in the image. Since the camera's field of view is limited to an area of 1 cm², records of larger samples are realized through rastering. The image is therefore composed of several square-shaped 'tiles'. The change in the inclination value at the tile borders visible as a sudden change in the gray value (see Figure 9, right panel, upper part) is caused by a systematic error of the G50 device that will be described in Section 4.1.2.

4.1.1 *Metric*

The azimuth and inclination are spherical coordinates of a unit vector in a 3D Euclidean space, which represents the *c*-axis of the crystal.

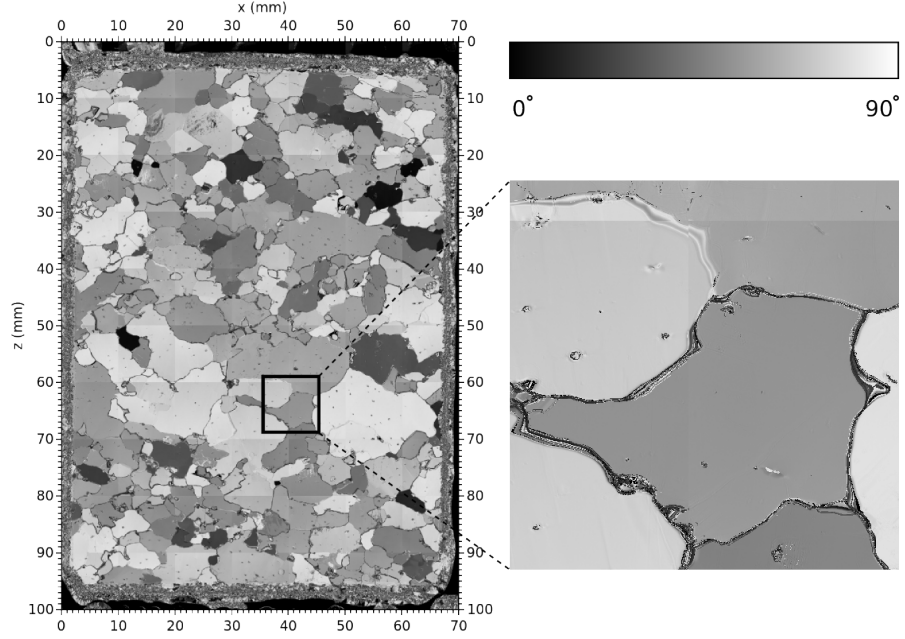


Figure 9: Inclination signal of a thin section taken from 784 m depth (NEEM 1426_201). The resolution is $20\ \mu\text{m}/\text{pixel}$ and the size of the measured area is $7\ \text{cm} \times 10\ \text{cm}$. The right image is a $1\ \text{cm}^2$ detail. White pixels illustrate shallow c -axes, parallel to the image plane; a black color represents steep c -axes, which are perpendicular to the image plane.

Each pixel in the fabric image represents therefore one c -axis vector. This metric is different from standard scalar pixel-type images or three-channel color images and this must be taken into account when applying DIP routines. The description through unit vectors is a kind of overdetermination because it gives an orientation to the c -axis, which is, however, arbitrary: In general, there are always two vectors \mathbf{c} and $-\mathbf{c}$ describing the same c -axis. For operations such as addition or dot product, the vectors should be selected in such a way that the angle between them is acute.

In a scalar-type pixel image, the difference between two pixels is given by the subtraction of their values. In an image consisting of unit vectors, the corresponding parameter is the angle between two pixels – called the *misorientation* γ ,

$$\gamma(\mathbf{c}_1, \mathbf{c}_2) = \arccos |\mathbf{c}_1 \cdot \mathbf{c}_2|. \quad (15)$$

The absolute value of the dot product asserts that $\gamma \in [0, \pi/2]$.

The same rule is applied also when calculating the average of two pixels. While in a grayscale image this is realized through the arith-

metric mean of the pixel values, here the average c-axis \mathbf{a} is defined as the normalized sum of the two vectors,

$$\mathbf{a} = \begin{cases} (\mathbf{c}_1 + \mathbf{c}_2) / |\mathbf{c}_1 + \mathbf{c}_2| & \text{if } \mathbf{c}_1 \cdot \mathbf{c}_2 \geq 0 \\ (\mathbf{c}_1 - \mathbf{c}_2) / |\mathbf{c}_1 - \mathbf{c}_2| & \text{if } \mathbf{c}_1 \cdot \mathbf{c}_2 < 0. \end{cases} \quad (16)$$

The misorientation angle and average axis are important measures for the image segmentation described in [Section 4.3.1](#).

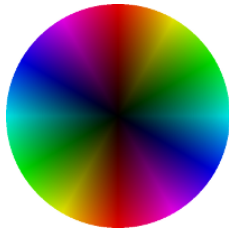
4.1.2 Error Estimation

Azimuth and inclination are determined separately by the G50 Fabric Analyser using different methods ([Section 3.2.2](#)). Due to this fact, different errors for the two angles are expected. In order to estimate the errors, measurements on quartz monocrystals with prepared orientations were performed. [Figure 10a](#) and [Figure 10b](#) show c-axes orientation images of a crystal with $\varphi = 0^\circ$, $\theta = 20^\circ$ and another one with $\varphi = 0^\circ$, $\theta = 70^\circ$ respectively.

The following errors in the azimuth and the inclination signal have been determined from the two measurements:

- The absolute error Δ is the difference between the average measured value and the theoretical orientation of the crystal. It can be caused by inaccurate positioning of the sample at the stage or by a systematic deviation produced by the device. An absolute error of the order of a few degrees is not important because the relative orientations within the sample are of interest, rather than the absolute orientation in space.
- The standard deviation σ is a measure of the noise of the signal. The standard deviation is computed from the twelve closest pixels for each point in the image.
- The gradient magnitude $|\nabla f|$ measures the variability of the signal f (i. e. the azimuth: $f = \varphi$, or inclination: $f = \theta$) as a function of the pixel coordinates. Although monocrystals with constant lattice orientation were used, the measured azimuth and inclination exhibit a dependence on the position in the image. This artificial gradient is a systematic error of the G50 device. It can be recognized by the color change in the color-coded c-axes images. On the border between the two tiles, the orientation gap can reach the order of several degrees of misorientation. For the gradient calculation, the images have to be Gaussian smoothed.

[Table 2](#) lists the average values of the three types of errors for azimuth and inclination as well as the corresponding misorientation angle γ . The absolute error in crystal orientation in both cases is less than 3° , which is a satisfactory value. The noise of the azimuth signal



Legend for background color

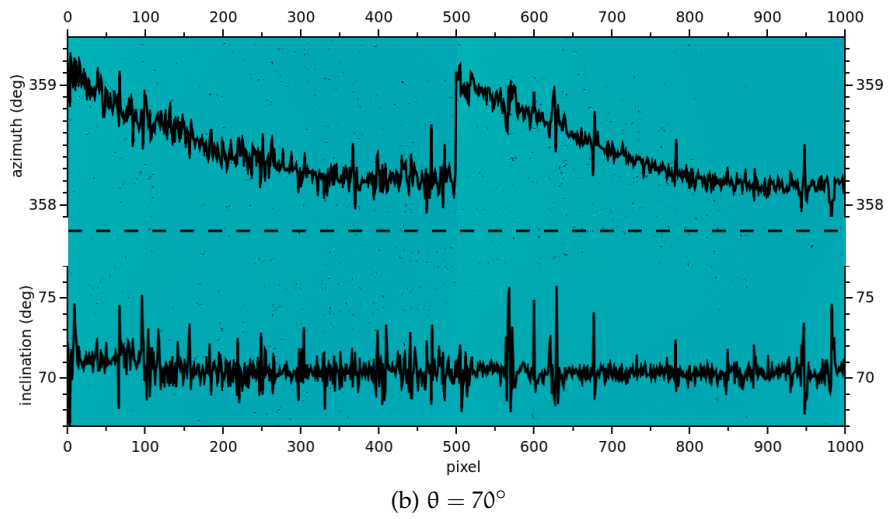
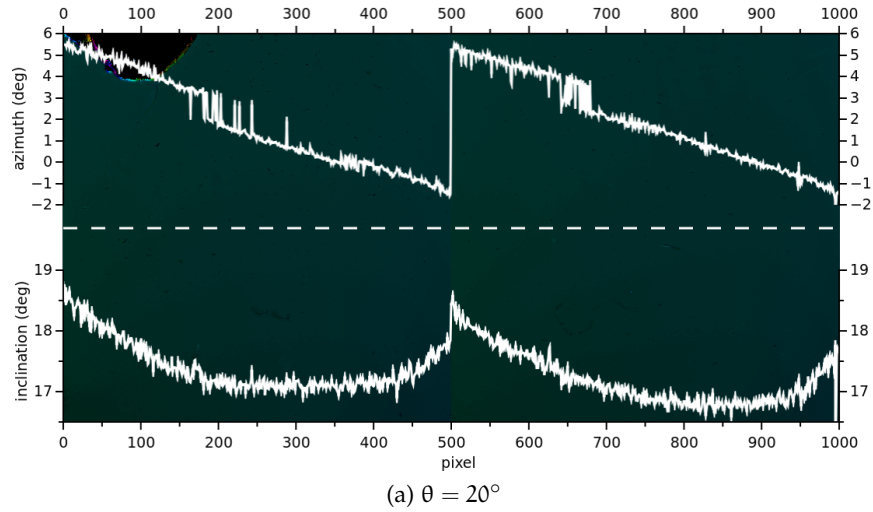


Figure 10: Two quartz single crystals with prepared lattice orientations. The resolution is $20 \mu\text{m}/\text{pixel}$. Each image consists of two tiles allowing to observe the signal behavior on the tile border. The azimuth and inclination signals measured along the dashed lines are plotted.

is higher at $\theta = 20^\circ$ than at $\theta = 70^\circ$, whereby the inclination noise exhibits an inverse behavior. The mean pixel misorientation, caused by the signal noise, increases with the c-axis inclination θ . The artificial gradient produces a mean change in orientation of 1.76° at a distance of 100 pixels.

SAMPLE 1	mean value (°)	Δ (°)	σ (°)	$ \nabla $ (°/100pix)
azimuth φ	1.85	1.85	0.22	2.06
inclination θ	17.31	2.69	0.08	0.54
misorientation γ		2.76	0.11	0.82
SAMPLE 2	mean value (°)	Δ (°)	σ (°)	$ \nabla $ (°/100pix)
azimuth φ	358.45	1.55	0.07	0.36
inclination θ	70.50	0.50	0.62	1.72
misorientation γ		1.55	0.62	1.76

Table 2: The absolute error, standard deviation, and gradient magnitude of the azimuth and inclination images with the corresponding misorientation angle.

4.1.3 Color Code

A commonly used method to plot c-axes orientations is the Lambert equal-area projection, which is an area-preserving (but not angle-preserving) mapping used in cartography. It projects the surface of a 3D unit sphere onto a circular area in a plane. A unit vector in spherical coordinates $\mathbf{c}(\varphi, \theta)$ is projected onto a 2D vector in polar coordinates $\mathbf{c}'(\varphi, r)$ with

$$r = 2 \cos \theta / 2. \quad (17)$$

Figure 11 illustrates the transformation of the inclination angle to the radius in polar coordinates. The c-axes are then represented through points within a circle. The circle corresponds to the maximal inclination of 90 degrees (see Figure 12b). This is referred to as a Schmidt diagram.

Although the thin sections are cut vertically (i.e. parallel to the core axis), the standard way is to project the c-axes in a horizontal reference frame (Durand et al. (2006)). The core axis (z-axis) is then represented through the center of the circle and the horizontal directions are assigned to the circle border. For the visualization of the c-axes orientations a color code has been implemented, based on the

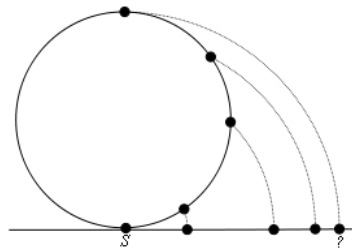


Figure 11: Lambert equal-area projection

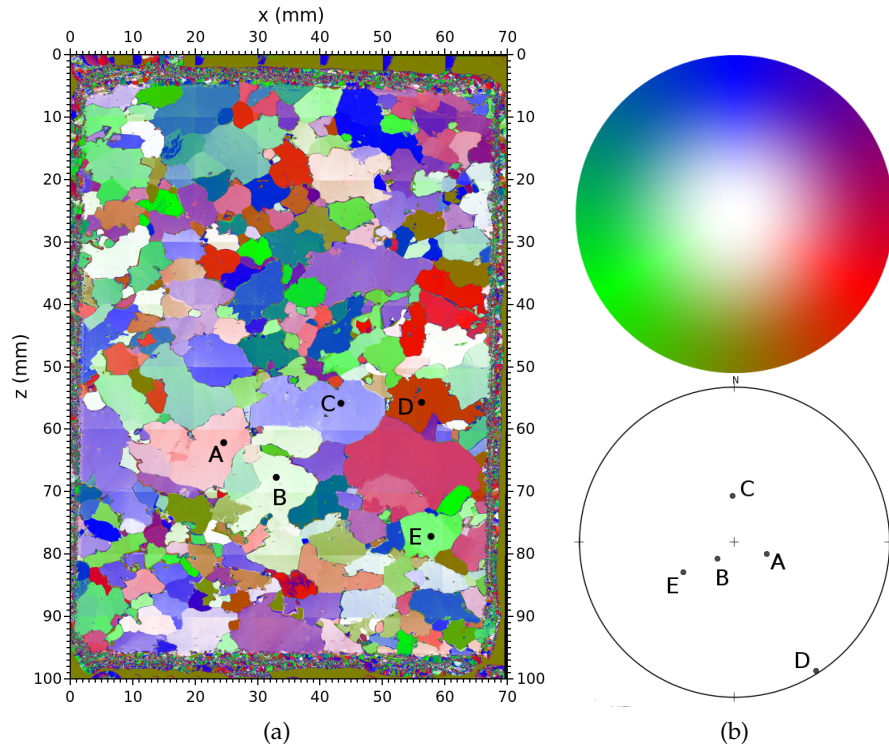


Figure 12: (a) Color-coded c-axes orientations of the same thin section (784 m) as in Figure 9. Five randomly chosen points (ABCDE) with different orientations are marked in the image. (b) The legend for the orientation color code and a Schmidt diagram with the five points, both based on the projection into the horizontal reference frame. Note that with this color code the Schmidt-diagram projection plane is perpendicular to the image plane.

projection into the horizontal reference frame. In this color coding, vertically oriented c-axes appear white and the horizontal directions are represented through the red-green-blue color cycle (Figure 12).

4.2 PREPROCESSING ROUTINES

4.2.1 Noise Reduction

The noise of the inclination signal increases with θ (Section 4.1.2). It produces a high mean pixel misorientation, which is not favorable for the edge detection, described in Section 4.3.1. In order to reduce the noise, an 8-neighborhood median filter is applied to the inclination signal. The advantage of median over average filters, such as Gaussian smoothing, is illustrated in Figure 13. In contrast to Gaussian smoothing, the median filter drops outlying pixels while conserving sharp edges.

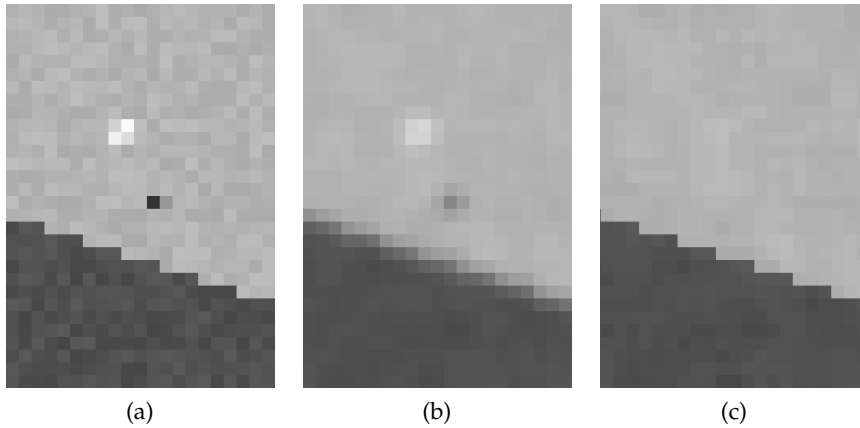


Figure 13: A gray-scale image (a) is smoothed by a Gaussian smooth filter (b) and a median filter (c). The squares represent individual pixels.

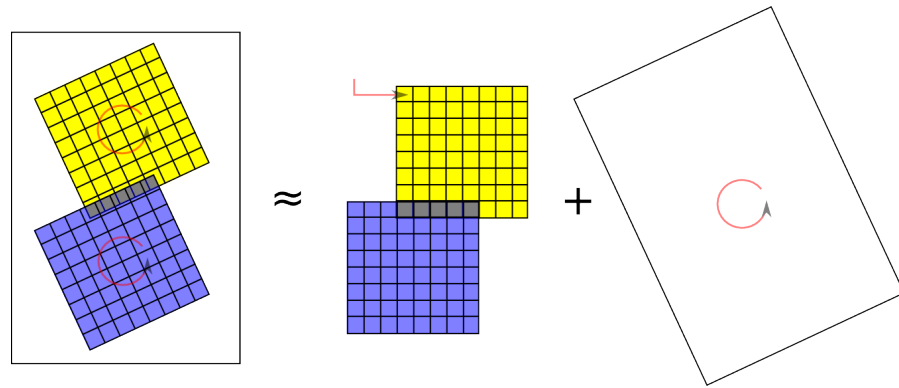
4.2.2 Tile Shift

Looking in detail at the original images (Figure 9, Figure 14b), there is always a tiny mismatch (of a few pixels) at the border between two tiles. Thin grain boundaries crossing the border suffer a discontinuity, which – in some cases – can lead to wrong grain detection in the main routine.

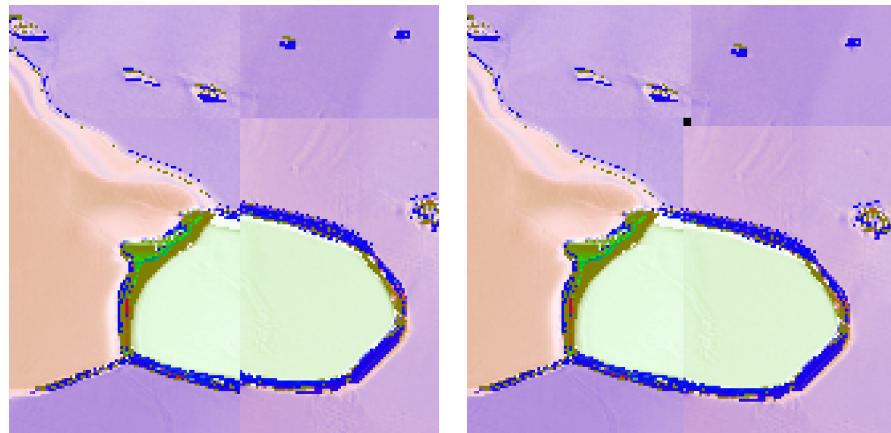
At first sight, the tile shift seemed to be a systematic error of the stage drives moving the sample. During measurements with the G50 in the ice laboratory, however, we noticed that a rotation of the camera with respect to the stage axes may be the main reason for this artifacts. The CCD camera is arranged by hand so that perfect adjustment can hardly be achieved. For tiles with a side length of 500 pixels, an adjustment error of only 1 degree will still produce a border mismatch of $\Delta_{\text{tile}} \approx 500 \cdot \sin 1^\circ \approx 8.7$ pixels.

In order to correct the data, the original image must be decomposed in tiles, each of them rotated around its center by a correction angle α and finally stitched again together, as illustrated in Figure 14a. This transformation can also be realized through a translation of individual tiles and a rotation of the whole image. If only discrete translations at pixel multiples are allowed, the raster structure remains consistent. Finally, for small α , the rotation part can be left out completely, since the alignment of the sample itself on the stage is not perfect (errors of the order of several degrees are expected).

In this way, a correction routine was implemented, which translates the tiles relatively to each other as if they would rotate around their centers, but without the necessity of image rescaling, which would be the consequence of real rotation. No automatic guess of the correction angle was implemented, with α being a parameter that has to be set by the program user. For the most NEEM ice core records a correction angle $\alpha = 0.4^\circ$ produced the best tile matches.



(a)



(b)

(c)

Figure 14: (a) Counterclockwise rotation of two tiles at $\alpha = 25^\circ$ can be realized through a tile translation and rotation of the whole image. (b) Detail of an original orientation image with a tile mismatch. (c) The corrected image with $\alpha = 0.4^\circ$.

4.3 MAIN ROUTINE: GRAIN NETWORK DETECTION

A polycrystal is composed of various crystals (grains) with different shapes and lattice orientations. Compared to the size of the crystals, interfaces between them (grain boundaries) are of infinitesimal thickness. The challenge of the main program routine is the recognition of grains and grain boundaries (image segmentation), followed by the determination of their orientation and shape parameters.

4.3.1 Image Segmentation

The basic assumption is that our images consist of two objects, namely grains and grain boundaries. Indeed, this is a strong simplification, since other image elements (e. g. air bubbles, fractures, subgrain structures etc.) are ignored.

Grain Detection

In the fabric image context, the grain may be defined as a *connected area of uniform c-axes orientation*. In fact, the connectedness of a volume only implies the connectedness of its section if the volume is convex. Thus we never know whether two separate areas with similar c-axes orientations represent two different crystals, or actually belong to the same non-convex grain.

Decomposition of an image into regions is called *segmentation*. A widely used method for region detection in scalar-type images is the determination of the image-gradient magnitude:

$$|\nabla| = \sqrt{(\partial/\partial x)^2 + (\partial/\partial y)^2}. \quad (18)$$

Points with low gradient values are grouped into regions, and points with high gradient values are classified as edges. Since our pixels represent unit vectors, an analogous method is to calculate the mean change in orientation (per pixel-length) for each point in order to decide, whether it belongs to the same region as its neighborhood or not. The first order approximation of the mean misorientation of a pixel at position ij is given through:

$$\langle \gamma \rangle_{ij} = \left[(\gamma(\mathbf{c}_{i,j}, \mathbf{c}_{i+1,j}) + \gamma(\mathbf{c}_{i,j}, \mathbf{c}_{i-1,j}))^2 + (\gamma(\mathbf{c}_{i,j}, \mathbf{c}_{i+1,j}) + \gamma(\mathbf{c}_{i,j}, \mathbf{c}_{i-1,j}))^2 \right]^{1/2}. \quad (19)$$

The resulting image can be seen as a topological relief with valleys representing regions with low neighbor misorientation – grains – and ridges indicating strong changes in crystal orientation – grain boundaries (Figure 15).

In the second step, a critical misorientation value γ_{\max} (threshold) has to be chosen. Points with $\langle \gamma \rangle < \gamma_{\max}$ are then interpreted as grain pixels, points with $\langle \gamma \rangle \geq \gamma_{\max}$ as lattice defect pixels. This procedure in image processing terminology corresponds to the generation of Watershed seeds. We can imagine it by filling the relief valleys with water up to the level of γ_{\max} . The separate lagoons mark the detected regions.

This segmentation process itself makes no restrictions of the segment size. A large number of regions consisting of only few pixels, or even single pixels with low mean misorientation will be detected and marked as regions. These segments obviously do not represent real grains. They are produced mainly by the volume effects of the image. The grain size, which can be measured by the fabric analyzer, has a lower limit, given by the thickness of the sample d . Grains with diameters smaller than d are hidden inside of the thin section and are therefore invisible. In order to discard the artificial regions, a minimal grain size A_{\min} has to be specified. In addition to the misorientation threshold γ_{\max} , this is another parameter required for the

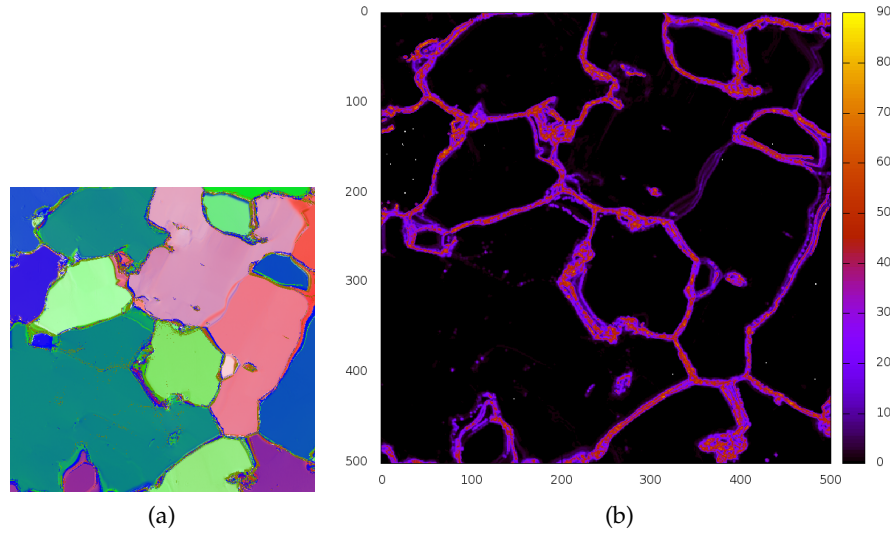


Figure 15: (a) One tile from the orientation image to be segmented. (b) Mean pixel misorientation calculated using Equation 19. Pixels with high misorientation with respect to their neighbors are assigned to grain boundaries

segmentation. Regions of area less than A_{\min} are removed from the list of detected grains. Figure 16a shows the detected regions applying $\gamma_{\max} = 1^\circ$. Figure 16b shows the same image after removing the smallest segments.

Boundary Detection

At this point, our image consists of a number of detected regions. The space between them is filled with pixels that were not attached to any grain. We now want to detect grain boundaries as thin paths between the regions. This is put into practice by letting the regions grow until they touch each other, with no space between them left.

Watershed region growing (Vincent and Soille, 1991) is a method that assigns pixels to available regions by means of a cost function f_c . For each region, a register of candidates exists, which lists all pixels at the region border. Candidates with low costs are attached first, the ones with high costs last. The candidate list is updated after each assignment of a pixel to a region. Two different cost functions were tested for our purpose:

1. $f_c = \text{const}$: The cost of all candidates is equal. The order of pixels in the candidate list is random, regions grow in a homogeneous way.
2. $f_c = \langle \gamma \rangle$: The candidates are sorted by their mean misorientation. In our relief analogy, this method corresponds to progressive flooding of the valleys until the whole landscape is under

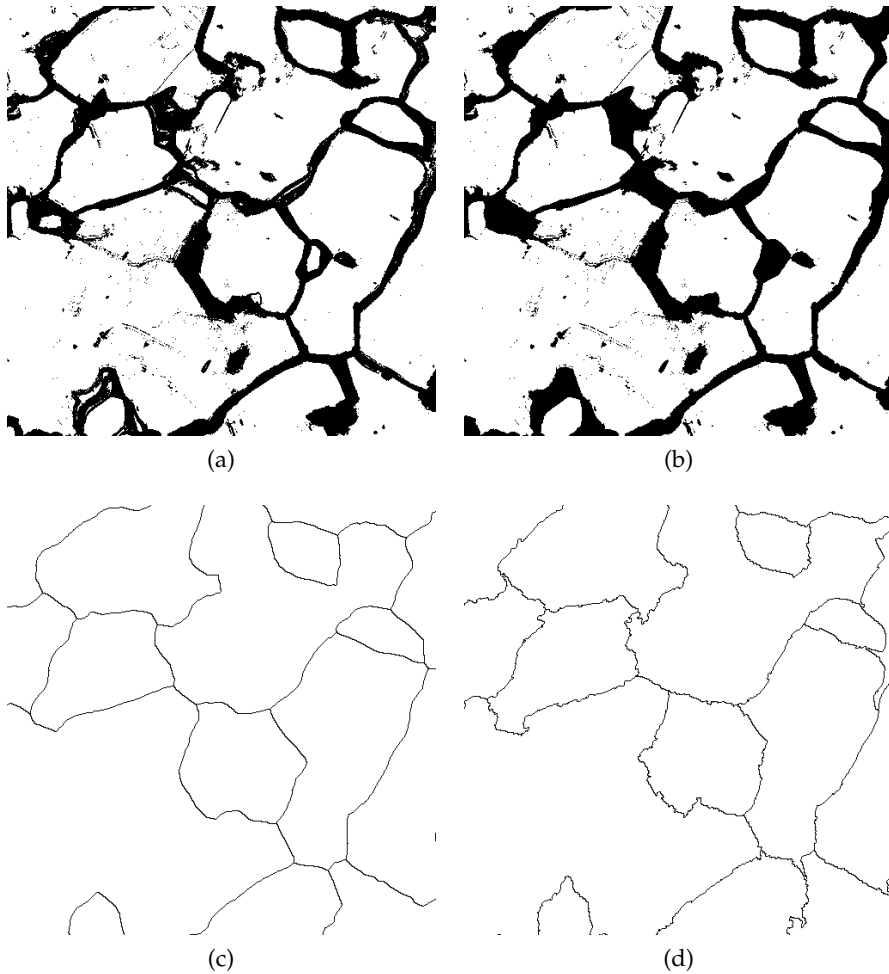


Figure 16: (a) Detected regions with $\gamma_{\max} = 1^\circ$. Pixels that do not belong to any region are marked in black. (b) The same image after removing segments smaller than $A_{\min} = 500 \text{ pixel} = 0.2 \text{ mm}^2$. (c) Grain boundaries obtained by homogeneous region growing and (d) by applying the Watershed flooding algorithm. One-pixel-wide black spaces were left between the grains in order to visualize the boundaries.

water. The positions, where individual lagoons get connected, are marked as grain boundaries.

Both region growing methods, applied to the initial regions from [Figure 16b](#), can be compared in [Figure 16c](#) and [Figure 16d](#). In general, grain boundaries detected through homogeneous region growing are smoother. This is in better agreement with the grain boundary shapes measured by other techniques such as [LASM](#). Therefore, the method of homogeneous region growing was implemented in the final program version.

4.3.2 Extraction of Parameters

For both image objects - grains and grain boundaries - a number of shape and orientation parameters is calculated by the program.

Grains

1. The grain cross-sectional area A is the number of pixels that form a grain. At a given image resolution, A can be expressed in mm^2 . Its lower limit is given through the segmentation parameter A_{\min} . The upper limit is the area size of the thin section.
2. The average c-axis vector is calculated for each grain using [Equation 16](#). It indicates the mean lattice orientation of a single grain.

Grain Boundaries

The grain boundary is a curve that connects two triple points (its end points) and separates exactly two grains. The existence of a common grain boundary is the condition for two grains to be called adjacent. The following parameters are extracted for each boundary by the program:

1. The length of the curve L is calculated by counting pixels between the end points:

$$L = \sum_i g_i \cdot \text{pixelsize}, \quad (20)$$

with $g = 1$ in case of a horizontal or vertical step, and with $g = \sqrt{2}$ in case of a diagonal step.

2. The linearity factor δ is a measure for the straightness of the curve. It estimates how well a grain boundary can be approximated by a straight line. It is calculated as the ratio of the distance d between end points and boundary length:

$$\delta = d/L. \quad (21)$$

The value range is $0 < \delta \leq 1$, with $\delta = 1$ for a straight line and $\delta \rightarrow 0$ for a closed curve.

3. The slope angle β is the angle between the image x-axis and the straight line connecting the grain-boundary end points a and b :

$$\beta = \begin{cases} 90^\circ & \text{if } x_a - x_b = 0 \\ \arctan \frac{y_a - y_b}{x_a - x_b} & \text{else.} \end{cases} \quad (22)$$

The range of possible values is $-90^\circ < \beta \leq 90^\circ$ with -90° and 90° both indicating the core axis direction.

4. The misorientation angle γ is the angle between the average c-axes \mathbf{c}_i and \mathbf{c}_j of two adjacent grains separated by the boundary. It is calculated using [Equation 15](#).
5. The rotation axis \mathbf{r} is the normalized cross product of the adjacent grains' average c-axes:

$$\mathbf{r} = \frac{\mathbf{c}_i \times \mathbf{c}_j}{|\mathbf{c}_i \times \mathbf{c}_j|}, \quad (23)$$

It is the normal vector of the plane in which \mathbf{c}_i is rotated into \mathbf{c}_j by the angle γ .

4.3.3 Segmentation Errors

The creation of artificial grain boundaries is the most frequent segmentation error. It occurs when a lattice orientation discontinuity that does not constitute a real grain boundary is misinterpreted as such during the segmentation routine. Such discontinuities appear at the borders between the square-shaped tiles due to the systematic error of the G50 Fabric Analyser described in [Section 4.1.2](#). Thus, during the creation of the misorientation-gradient image in the segmentation routine individual tiles are treated separately, omitting the tile borders.

Two other common sources of artificial discontinuities are *fractures* and *microtome scratches* on the surface of a thin section ([Figure 17](#)). Sample fractures can be created during the whole process of thin sec-

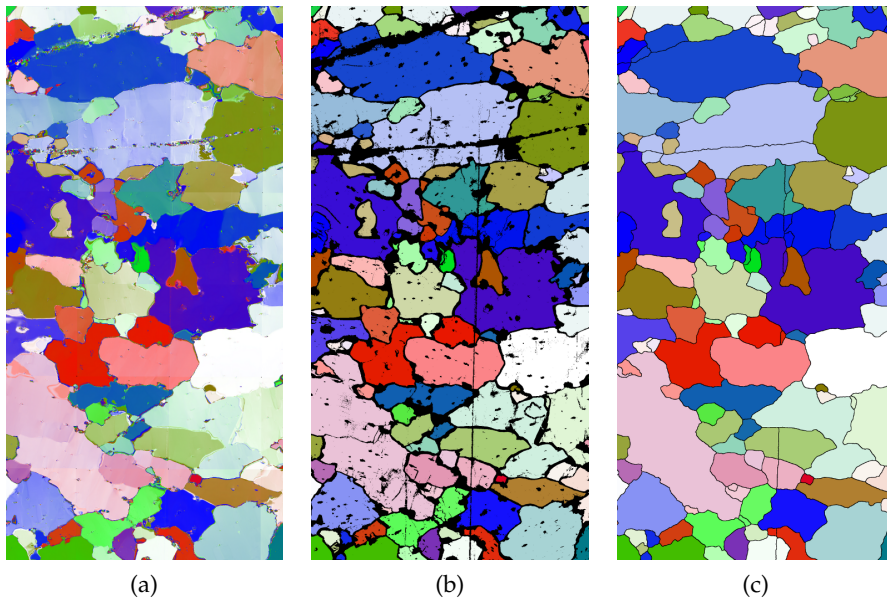


Figure 17: Segmentation of the fabric image of a thin section from 1026 m below surface which contains both – scratches and fractures.

tion preparation. They produce a long wide stripe of pixels with random orientations across the whole image. After segmentation, a chain of artificial grain boundaries with similar orientations is present.

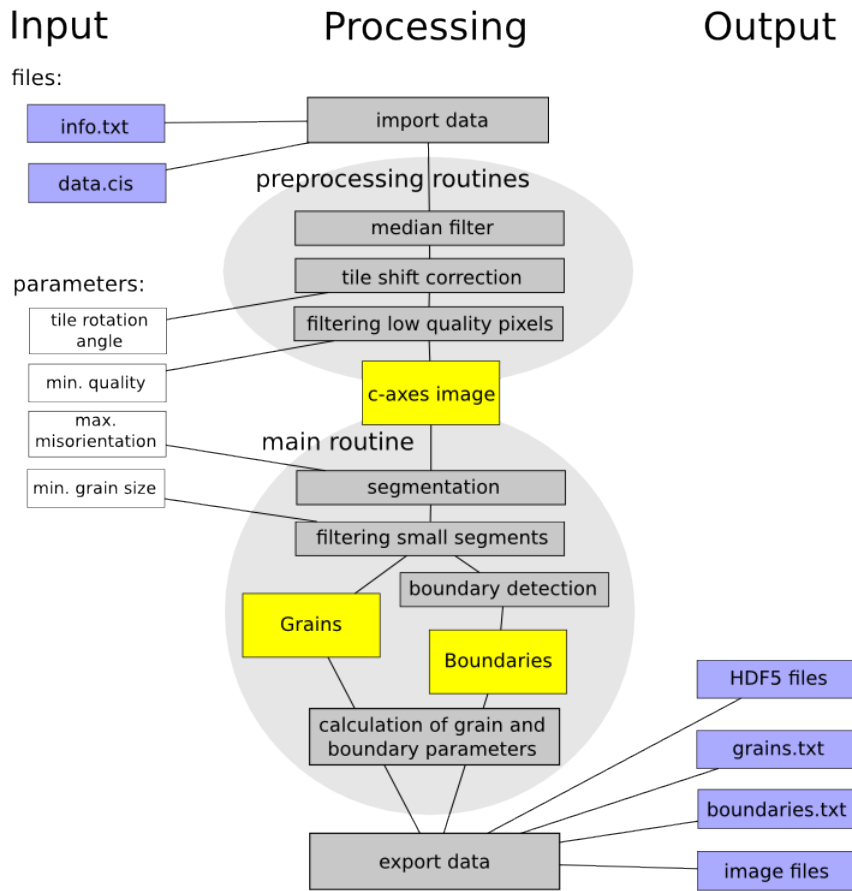
Vertical scratches on the sample surface may be produced by a microtome with an unsharp blade. They can be hardly recognized in the orientation image, but during segmentation with a low misorientation threshold γ_{\max} they are detected and interpreted as straight vertical grain boundaries.

In order to avoid the detection of artifacts as grain boundaries, an additional criterion is necessary. For the microtome scratches, this would be a combination of the straightness, verticality, low misorientation, and the appearance in a chain crossing the whole sample. An automatical recognition of such image artifacts has been left for future implementations.

4.4 PROGRAM EXECUTION

cAxes is a command-line-operated program. After inserting the input parameters and the path to the source data, the execution runs automatically. Alternatively, a list of source paths can be passed to the program so that many fabric data can be processed in a queue using the same segmentation parameters. [Figure 18](#) shows a diagram that illustrates the functionality of the program. After the *c*-axes orientations are imported from the G50-device data file, an orientation-image structure is created. The image is decomposed into individual tiles and the preprocessing routines are applied - i. e. the median filter and tile shift correction. In the next step, the segmentation routine detects grains and boundaries by means of the mean misorientation $\langle\gamma\rangle$. The size, shape, and orientation parameters are calculated for all detected grains and grain boundaries. Finally, several output files are created. The grains and boundaries are saved separately in two text files, which contain a list of the detected objects and the corresponding extracted parameters. Three color-coded images are exported containing the original orientation image (*vectorimage_rgb.png*), the image after segmentation (*grains_rgb.png*), and the grain boundary network after region growing (*boundary_rgb.png*). The segmentation results are also saved in a HDF5 file for further processing.

[Table 3](#) summarizes the input parameters required by the program before a segmentation run. The right column lists the parameter values that were used for the processing of the [NEEM](#) ice core data recorded by the [AWI G50](#) device. The results of the analysis are discussed in the next chapter.

Figure 18: *cAxes* program execution diagram.

Parameter	Description	Value used
gq_{\min}	minimal geometrical quality	50%
rq_{\min}	minimal retardation quality	50%
γ_{\max}	misorientation threshold for the image segmentation	1°
A_{\min}	minimal size of a region to be considered as a grain	500 pix
α	rotation angle for the tile-shift correction	0.4°

Table 3: Program input parameters.

RESULTS: APPLICATION TO THE NEEM ICE CORE

This chapter presents the results of the c-axis analysis of the [NEEM](#) ice core (Greenland). First, a short introduction of the [NEEM](#) ice core is given. [Section 5.2](#) presents the results of the analysis of c-axes-orientation distributions. This corresponds to the conventional treatment of fabric data in order to describe the anisotropy variation with depth. The subsequent two sections use more innovative approaches to study the misorientation angles between adjacent grains ([Section 5.3](#)) and the shapes and preferred directions of grain boundaries ([Section 5.4](#)).

5.1 THE NEEM ICE CORE

The North Greenland Eemian Ice Drilling ([NEEM](#)) is an international ice-core project led by a Steering Committee consisting of 14 countries. A 2540 m long ice core was drilled between 2008 and 2011 through the ice sheet down to the bedrock. The location of drilling (77.45° N, 51.06° W) was selected with the purpose to obtain an undisturbed northern hemisphere ice-core record covering the last interglacial period – the Eemian. The Eemian ice found in previous Greenland ice cores, such as NorthGRIP, was garbled and incomplete due to basal melting.



Figure 19: The NEEM ice-core drilling location, taken from the [NEEM website \(2013\)](#).

Fabric Data

More than 700 fabric images have been recorded along the NEEM ice core between 2009 and 2011. Four different FA devices have been operated (AWI, NIPR, CPH, LGGE) for this purpose by German, Japanese, Belgian, Danish, and French scientists. The ice core has been cut in 55 cm long pieces (also called bags) for easier handling, storage and transport. For the fabric analysis, each of the pieces is cut into six parts for the preparation of thin sections. The results presented below are based on the processing of 389 thin sections. The sections that could not be analyzed here are either special measurements with varying resolutions or show artifacts of one FA device (NIPR) described by Surma (2011). Between 2000 and 2100 meters no measurements are available. At this point I would like to express my gratitude for the possibility to benefit from this large set of data that were recorded under extreme conditions by others.

5.2 CLASSICAL ANALYSIS: ANISOTROPY

5.2.1 Preliminaries

Structural geology describes a large number of crystal orientation distributions and transitions between them (Wallbrecher, 1986). Here the three basic patterns shall be introduced which occur in ice and are easy to describe by the 2nd order orientation tensor (see below).

1. Isotropic (uniform) distribution is present if grains are oriented in all directions with the same probability. In the Schmidt diagram, the density of data (i. e. the number of points per unit area) is then constant.
2. Cluster distribution occurs whenever there is a preferred crystal orientation. When clustering is so strong that in effect all crystals align in the same direction, we speak of a single maximum pattern. In ice, the c-axes tend to align along the compression axis. Thus a single maximum indicates the direction of uniaxial compression.
3. Girdle fabric is an axially symmetric pattern, in which the c-axes are distributed on a great circle of the unit sphere. It can be interpreted as the opposite to a cluster.

Various statistical parameters have been introduced in the past with the purpose to quantify alignment strength in fabrics. Many of them, such as the *fabric strength*, *concentration parameter*, *spherical aperture*, etc. (Adam, 1989), are based on the calculation of the c-axis sum vector

$$\mathbf{s} = \frac{1}{n} \sum_{i=1}^n \mathbf{c}_i, \quad (24)$$

with \mathbf{c}_i being the c-axis vector of the i^{th} grain and n the total number of grains. The larger the norm of the sum vector \mathbf{s} , the stronger is the c-axes alignment. If all axes lie parallel to each other, then $|\mathbf{s}| = 1$. The advantage of the sum vector norm is its simplicity: only one number describes the whole orientation statistics. The two disadvantages are:

1. The sum vector norm only estimates the strength of the c-axes alignment. Other distribution besides a single cluster are not well described.
2. The sum vector is *not* invariant of the reference frame. Its norm and orientation depend on the way we choose the c-axis vectors (\mathbf{c} or $-\mathbf{c}$, see [Section 4.1.1](#)). This property does not seem desirable for an objective analysis.

A more general way to describe axial distributions is the determination of orientation tensors. The orientation tensor of k^{th} order is given through

$$\mathbf{A}^{(k)} = \frac{1}{n} \sum_{i=1}^n \mathbf{c}_i^{\otimes k} = \sum_{i=1}^n \underbrace{\mathbf{c}_i \otimes \mathbf{c}_i \otimes \dots \otimes \mathbf{c}_i}_k. \quad (25)$$

The sum vector from [Equation 24](#) is thus the 1st-order orientation tensor. [Durand et al. \(2006\)](#) conclude that the dependency on the reference frame (mentioned above for the sum vector) is a common characteristic of all odd-order orientation tensors. In contrast, even-order orientation tensors are invariant under the choice of c-axes vector orientations. The authors therefore suggest that only even-order orientation tensors should be used for fabric analysis.

The 2nd-order orientation tensor is used for fabric analysis in this thesis. This method was introduced in geology by [Scheidegger \(1965\)](#) and is analogous to the calculation of the inertia matrix of a system, where c-axes are represented through mass points on the surface of a unit sphere. The eigendecomposition of the matrix defines the inertia ellipsoid with the *eigenvectors* $\mathbf{e}_1, \mathbf{e}_2, \mathbf{e}_3$ and the *eigenvalues* $\lambda_1, \lambda_2, \lambda_3$ defining the principal axes directions and lengths respectively.

[Gagliardini et al. \(2004\)](#) proposed to weigh each grain by its cross-sectional area A . The sum of eigenvalues of the normalized orientation tensor (i. e. the trace of the matrix) is equal to one:

$$\lambda_1 + \lambda_2 + \lambda_3 = 1. \quad (26)$$

The following relations between the eigenvalues characterize the three fabric prototypes introduced above:

Of course, general distributions have the shape of a tri-axial ellipsoid ($\lambda_1 < \lambda_2 < \lambda_3$), with a weaker or stronger tendency towards one of the ideal types. In order to distinguish between cluster and gir-

eigenvalues	inertia shape	distribution
$\lambda_1 = \lambda_2 = \lambda_3 = 1/3$	sphere	uniform distribution
$\lambda_1 = \lambda_2 < \lambda_3$	prolate ellipsoid	unimodal cluster
$\lambda_1 < \lambda_2 = \lambda_3$	oblate ellipsoid	girdle fabric

dle fabrics, Woodcock (1977) introduced the parameter κ (Woodcock parameter) as follows:

$$\kappa = \frac{\ln(\lambda_3/\lambda_2)}{\ln(\lambda_2/\lambda_1)}. \quad (27)$$

Distributions with $\kappa > 1$ are classified as clusters, those with $\kappa < 1$ as girdles.

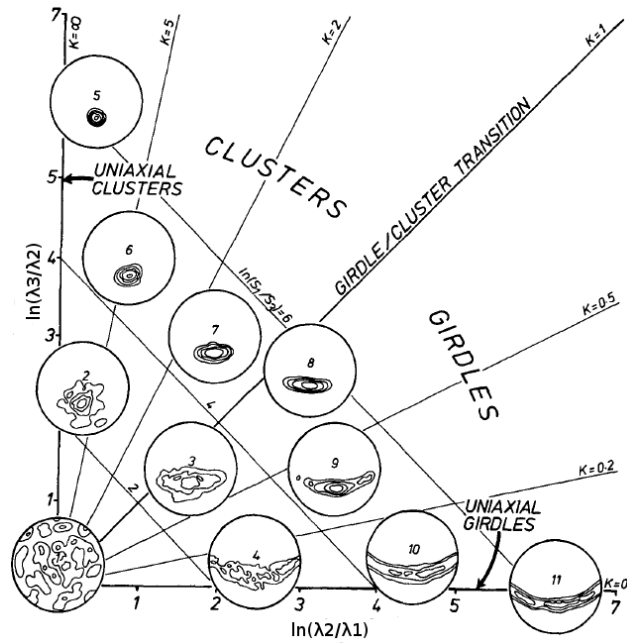


Figure 20: Logarithmic plot of ratios of normalized eigenvalues, taken from Woodcock (1977).

5.2.2 Variation over the Whole Core Length

Figure 21 shows the orientation tensor eigenvalues over the whole ice core length. All data are based on grain area weighted statistics. The variation of the mean grain size and the Woodcock parameter in comparison to the eigenvalues is shown in Figure 22.

In the first 1400 meters the fabric development is in a good agreement with the observations made on other ice cores from similar locations, such as the NorthGRIP (Wang et al., 2002). With increasing depth, crystals progressively align along the core axis. This is typical

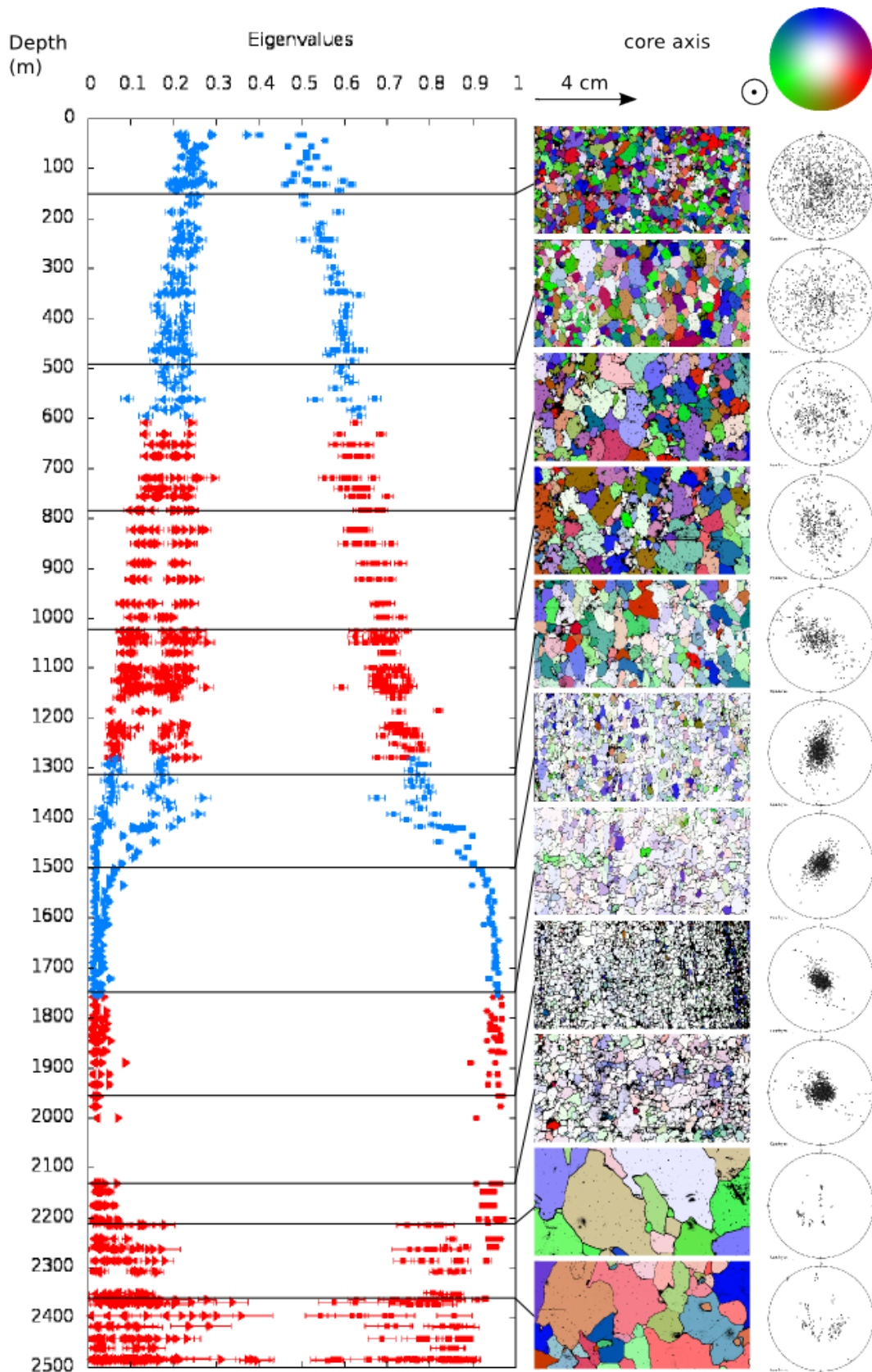


Figure 21: Orientation-tensor eigenvalues along the NEEM ice core. Red points represent thin sections measured with the AWI G50, blue points those measured with the LGGE instrument. The error bars correspond to the sampling error estimation proposed by Durand et al. (2006). At the right side, fabric images of eleven randomly chosen thin sections from different depths are presented. The corresponding Schmidt diagrams, presented on the right, show the average c-axes of individual grains projected onto the horizontal plane.

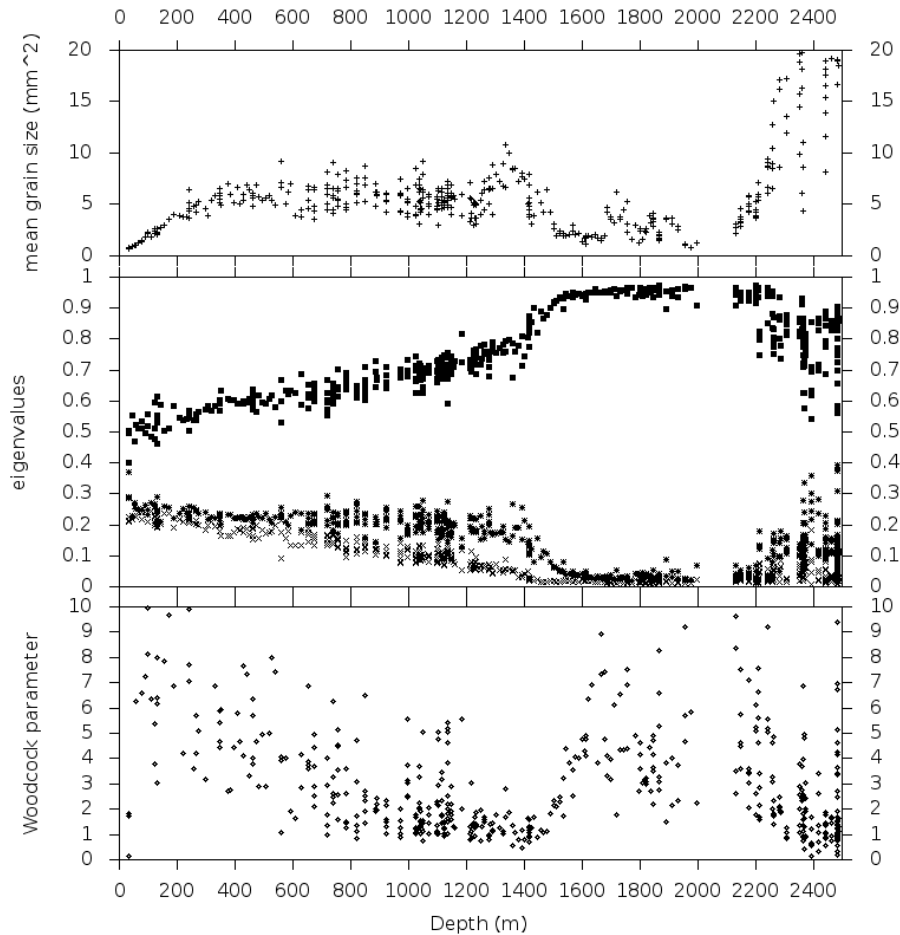


Figure 22: Variation of the mean grain size, $\mathbf{A}^{(2)}$ eigenvalues, and Woodcock parameter along the whole ice-core depth.

for a deformation mostly driven by uniaxial compression along the vertical direction. Starting at around 700 meters, the development of a weak girdle fabric is evident (Woodcock parameter less than 1). The highest eigenvalue exhibits a nearly linear increase with depth, starting with $\lambda_3 \approx 0.5$ at 30 m and reaching $\lambda_3 \approx 0.75$ at 1400 m. Note that even in layers very close to the surface, the orientation tensor eigenvalues do not indicate a perfectly uniform orientation distribution. This is in accordance with some recent studies on snow that propose the possibility of preferred crystal orientations being relevant already during the accumulation and densification processes (Riche et al., 2013). The linear increase in the average grain size due to *normal grain growth* stops between 300 and 400 meters. In the classical view this is explained through the activation of *rotation recrystallization*. This model is called into question in Section 5.3.

Around 1400 meters of depth, an abrupt transition to a strong single maximum is observed. Below this depth down to 2200 meters, most grains are vertically oriented (appearing white in the color code), with the highest eigenvalue reaching $\lambda_3 \approx 0.95$. This is corre-

lated with a significant decrease in average grain size (Figure 22) and a higher content of dust (unpublished data) which is typical for the Ice Age ice. A similar collapse of the girdle fabric into a strong single maximum has been observed in the NorthGRIP ice core as well. However, in NEEM it occurs at a much shallower depth (NEEM 1400-1600 m; NorthGRIP 2000-2500 m). The peculiarity of NEEM is that this feature overlaps with the transition between the last *Glacial* period and the present interglacial *Holocene*. The correlation between the change in c-axes alignment and the climatic transition can be attributed to the impact of the stress shear component in combination with different viscosity of Glacial ice.

The next change in the fabric pattern appears at around 2200 meters. This change is also related to a climatic transition, namely to the transition between the Glacial and last interglacial period – the *Eemian*. The single maximum disappears and crystals exhibit a high variety of orientations. The grain size shows a very strong increase reaching the limits of the thin sections, which implies that only few grains can be recorded. Due to this limitation, the statistical results in the deepest parts of the ice core (Eemian) are of lower confidence. Moreover, average grain size and eigenvalues show high variabilities from bag to bag and within bags, which is due to the mixture of layers in folded ice (NEEM community members, 2013) as well as deformation effects during folding. The probable original stratigraphic sequence of the Eemian ice could be reconstructed from global atmosphere markers in the disturbed layering for the first time for a deep ice core by NEEM community members (2013). Preliminary results from this thesis support this pioneering study (NEEM community members, 2013, Fig. 3c and 3d).

5.2.3 High Resolution Studies

In the previous part, eigenvalues of the second order orientation tensor were calculated for each thin section. A different approach is to study the variation of the crystal-orientation distribution over short distances within the thin sections. For this purpose, I implemented a realization of the running-mean method. In this scope, the statistical parameters (eigenvalues, mean grain size, number of grains) are calculated within a small frame in the image. Continuous change of the frame position allows to plot the variation of the parameters within a thin section or along several connecting sections (Figure 23). The vertical and horizontal size of the rectangular frame can be chosen as well as the step width by which it glides over the sample image. Its size should be chosen in such a way that it still contains enough grains for the statistical evaluation.

Tammen (2012) used this method in her bachelor thesis to study correlations between the mean grain sizes and the eigenvalues of the

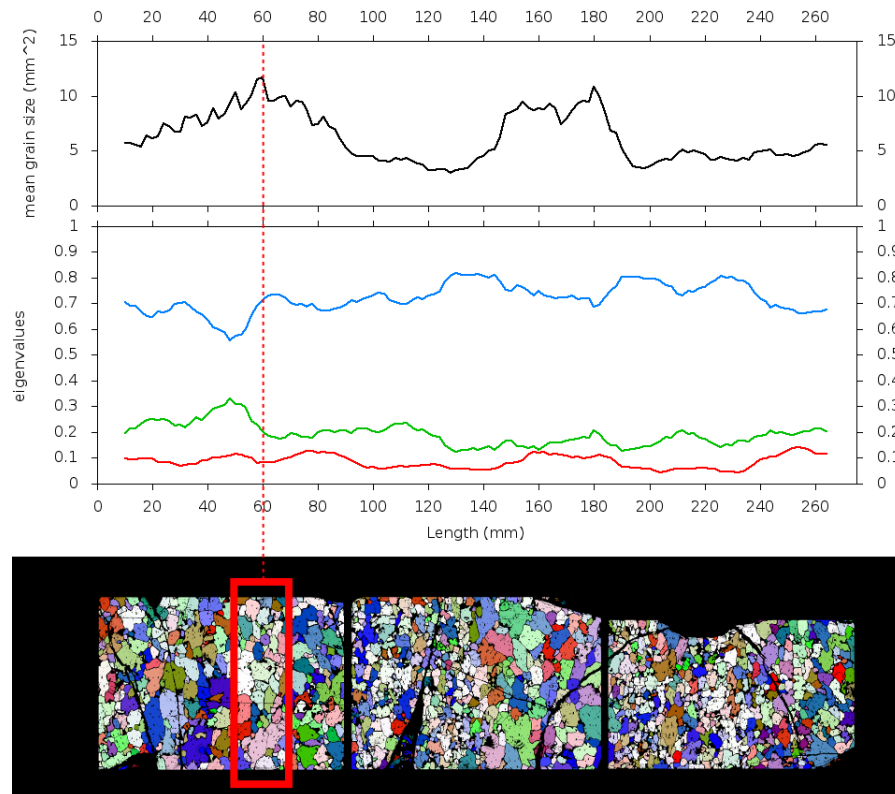


Figure 23: Running mean over three connecting thin sections from 1026-m depth. Average grain size and eigenvalues of the orientation tensor are calculated within the red frame.

orientation tensor. Although, only weak correlations could be found in general, there is a difference between Holocene and Glacial ice. While Holocene ice exhibits a negative correlation between the grain size and the highest eigenvalue, the correlation in Glacial ice is positive (Figure 24).

5.3 MISORIENTATION BETWEEN ADJACENT GRAINS

The automatic detection of grain boundaries (GB) allows to study relations between adjacent grains. In this section, the misorientation between neighboring crystals is analyzed. It is assumed that physical interactions between adjacent grains due to recrystallization processes would leave a characteristic mark in the intergranular misorientations (Wheeler et al., 2001). The previous studies of grain misorientations in ice were limited to a few thin sections (Alley et al., 1995; Durand et al., 2008). The automatic recognition of grains and grain boundaries allows to perform a systematic evaluation of the misorientation distribution along the whole NEEM ice core.

Figure 25 shows the neighbor-pair misorientation distribution over the ice core length. It can be interpreted as the Probability Density

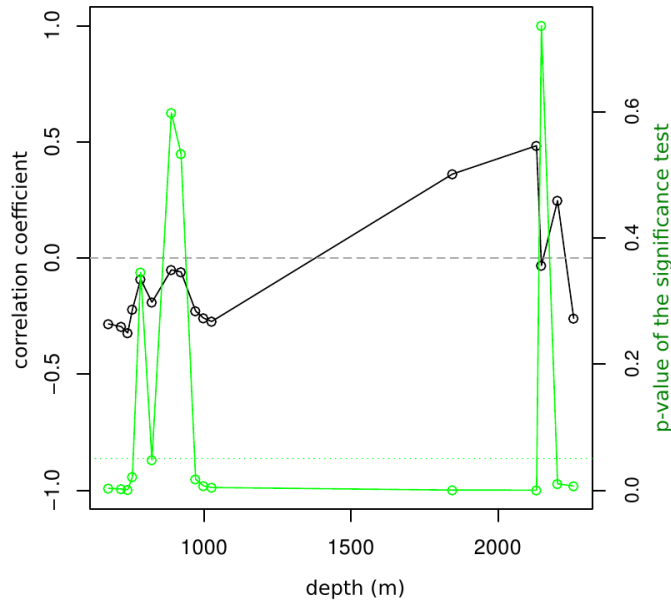


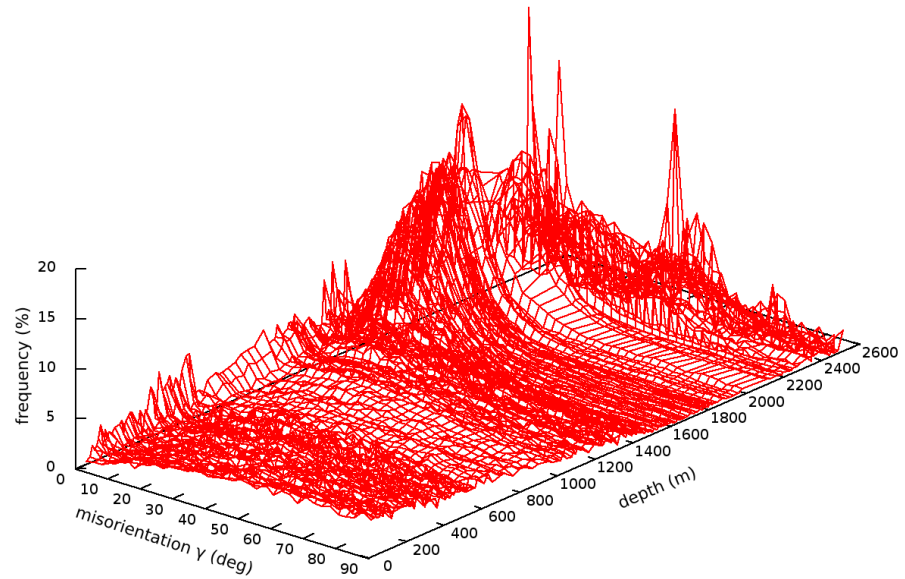
Figure 24: Correlations between highest eigenvalues and grain sizes taken from [Tammen \(2012\)](#).

Function (PDF), $p(\gamma)$, describing the relative likelihood of finding a neighbor-pair with misorientation γ . In the first part of the ice core, we observe a moderate progress towards lower angles with increasing depth. At a depth of 1400 meters - the Holocene-Glacial transition - a strong maximum for misorientations around $\gamma \approx 10^\circ$ develops. GBs with misorientations higher than 40° are virtually not present. This pattern is characteristic for the whole Glacial zone. With the transition to the Eemian, higher angle neighbor-pair misorientations appear again.

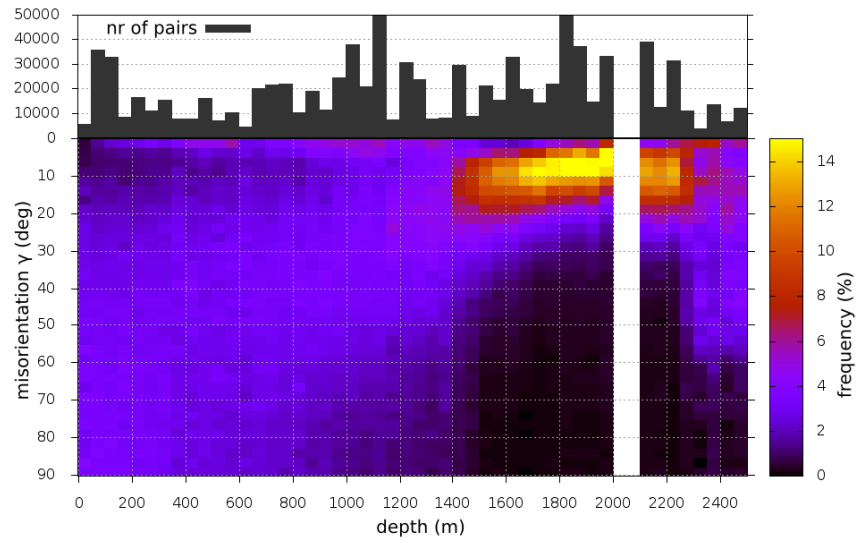
It is obvious that the misorientation PDF is directly connected to the c-axes orientation distribution described in [Section 5.2](#). In order to derive the probability of misorientation between two randomly chosen grains, one would have to integrate all possible orientations of the two c-axes with the appropriate orientation probabilities. This is trivial for the uniform c-axes distribution, where the orientation PDF $p(\varphi, \theta)$ corresponds to the surface of a three-dimensional half-sphere (see [Appendix A](#)). The normalized misorientation PDF for $0^\circ \leq \gamma \leq 90^\circ$ is then given by

$$dp(\gamma) = \sin \gamma d\gamma. \quad (28)$$

We can observe the sine-shaped γ -distribution in [Figure 25a](#) in the layers next to the surface, where the c-axes are (almost) randomly distributed. The analytical derivation of the misorientation-PDF for complex c-axes distributions is more demanding.



(a)



(b)

Figure 25: Adjacent-grains misorientation distribution. The upper image (a) is a 3D plot, where lines parallel to the misorientation axis represent the results of averaging over one bag. The lower image (b) is a color-coded histogram of the same data, with the distributions along the ice-core depth calculated in steps of 50 meters. The numbers of measured pairs (represented by the block bars on top) indicate the statistical weights.

Alley et al. (1995) proposed to estimate random-pair misorientation distributions using a Monte-Carlo simulation. The authors analyzed thin ice sections from the Byrd Station (West Antarctica) ice core selecting 10 000 random grain pairs and measuring their misorientations. Significant differences between the neighbor-pair PDF and the random-pair PDF imply physical interaction between adjacent grains occurring due to recrystallization. Durand et al. (2008) applied a similar method to the records of the upper 900 meters of the NorthGRIP ice core. The authors demonstrated the presence of rotation recrystallization through the higher occurrence of low-angle boundaries with respect to the simulated random-pair misorientation distribution.

In order to study the impact of physical interactions between adjacent grains, I generated 10 000 random grain pairs for each fabric image by reshuffling the existing grains. The random-pair misorientation distributions are shown in Figure 26 as a function of depth. The differences $p(\gamma)_{\text{adjacent}} - p(\gamma)_{\text{random}}$ between the neighbor-pair and the random-pair misorientation distributions are shown in Figure 27. Blue areas indicate intergranular misorientations, which appear with higher frequency than expected from the Monte-Carlo simulations. We observe a continuous cumulation of low angle boundaries along the ice core, which implies the presence of *rotation recrystallization*. It should be mentioned that a large amount of artificial GBs, generated during the segmentation as a product of fabric image artifacts (such as microtome scratches and fractures, see Section 4.3.3) would cause a high occurrence of misorientations equal or close to zero degrees. Although the systematic check to identify such artifacts could not yet be implemented due to thesis-time constraints (Section 4.3.3), visual inspection of the segmentation results¹ as well as the observation of

¹ Ca. 1 of 10 section contains such artifacts; samples with a high frequency of artifacts were excluded from the statistics.

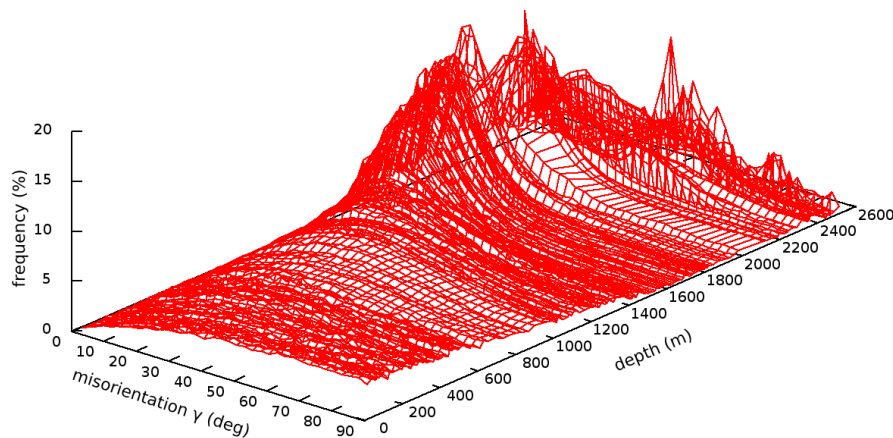


Figure 26: Random pair misorientation distribution

signal continuity towards higher angles strongly suggests that the cumulation is based on real grain boundaries.

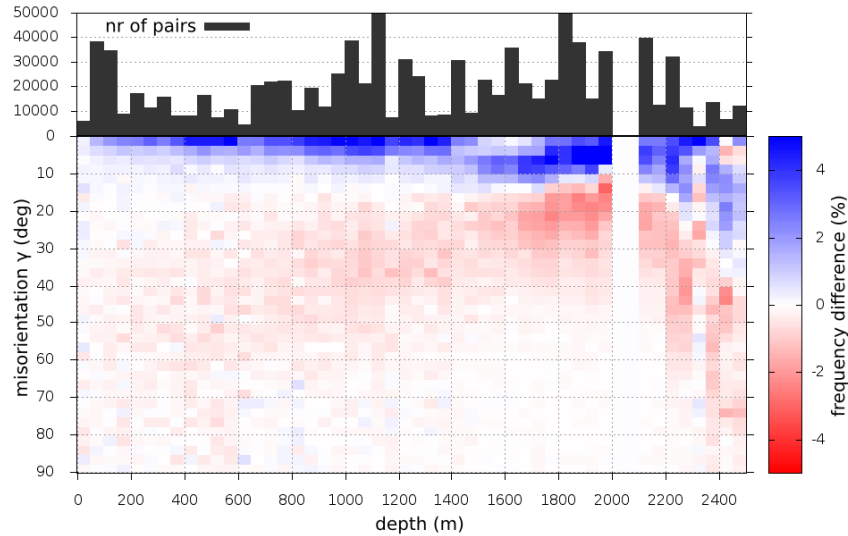


Figure 27: Difference between adjacent-grains misorientation distribution and Monte-Carlo-simulated pair misorientation distribution. Positive values (blue) indicate adjacent-grain misorientations that are more frequent than random-pair misorientations.

The presented results indicate that *rotation recrystallization* sets in already within the first 100 meters below surface. This confirms the conclusions of Durand et al. (2008) made on the NorthGRIP ice core and also contradicts the classical view, which assumes *rotation recrystallization* to be dominant within a limited zone and to be responsible for the *normal-grain-growth* interruption.

An interesting misorientation signal is observed in the Glacial ice (1400 m – 2200 m). The strong blue maxima do not rise with the very lowest angles as they do in the *Holocene*, but rather misorientations around 10° are cumulated. This may indicate a partition of the rotation recrystallization process, such that a halt of initial polygonization (formation of new boundaries; Figure 5 a&b) occurs while existing subGBs develop towards high angle GBs by further dislocation incorporation (Figure 5 c&d).

The increase of the dominance region from 10° to 40° in the lowest part of the core (2100-2500 m depth) may be related to the formation of a "diamond pattern" in Schmidt diagrams (Azuma and Higashi, 1985), which probably evolves due to an energy optimum of the intrinsic grain-boundary energy at about 40° (Suzuki, 1970).

5.4 GRAIN BOUNDARY GEOMETRY

This section analyzes the orientation and geometry of grain boundaries (GB). First, the absolute orientations in the image reference

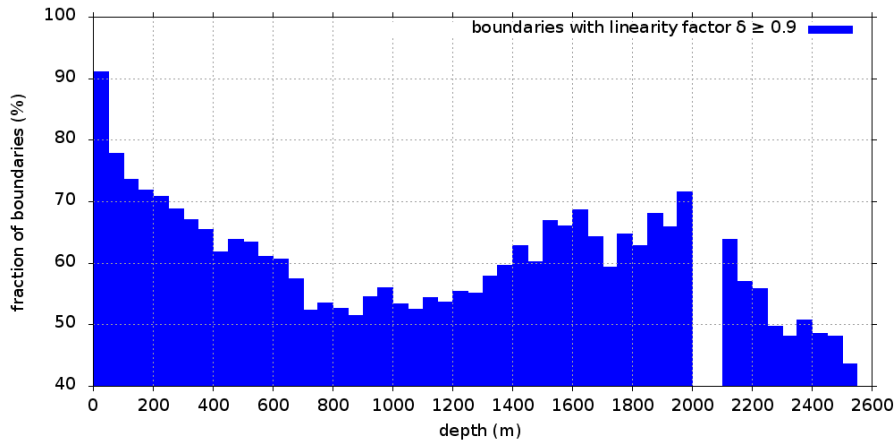


Figure 28: Fraction of grain boundaries with linearity factor $\delta \geq 0.9$ over the whole ice core length.

frame are discussed, followed by an analysis relative to the adjacent-grains crystallography.

The mean orientation within the image plane is calculated and expressed through the slope angle β (Section 4.3.2) for each GB detected by the program. This average orientation, indeed, is a good parameter to describe straight boundaries, but it loses its signification by increasing GB curvature. For a grain boundary starting and ending in the same point (i. e. surrounding an isolated grain), β has no meaning at all. Thus, the analysis presented below considers only (nearly) linear GBs with the linearity factor $\delta \geq 0.9$.

The percentage of straight grain boundaries ($\delta \geq 0.9$) along the NEEM ice core is plotted in Figure 28. In shallow depths, near the firn-ice transition, a great majority of GBs exhibit a straight shape. This is favorable in terms of the reduction of the GB-interface energy. With increasing depth the amount of irregularly shaped boundaries rises. It can be interpreted as an increasing impact of the GB-migration recrystallization driven by the stored strain energy (Weikusat et al., 2009). The fraction of straight GBs reaches a minimum ($\approx 50\%$) between 700 and 1200 meters (the brittle zone). A new increase marks the transition to the single maximum around 1400 m (which is correlated with the Holocene - Glacial transition). The Ice Age ice is characterized through a relatively high percentage of straight boundaries, which in combination with the strong c-axes alignment suggests a lower impact of GB migration recrystallization. The transition to the Eemian is than connected with a relative increase of curved boundaries and thus possibly a new activation of migration recrystallization.

Figure 29 shows two ice samples from different depths with the detected grain boundaries (black) and the color-coded mean grain orientations. The distribution of the GB slope angle β is plotted in the corresponding diagrams below. While the first sample (675 m) exhibits a rather uniform distribution, in the second sample (1787 m)

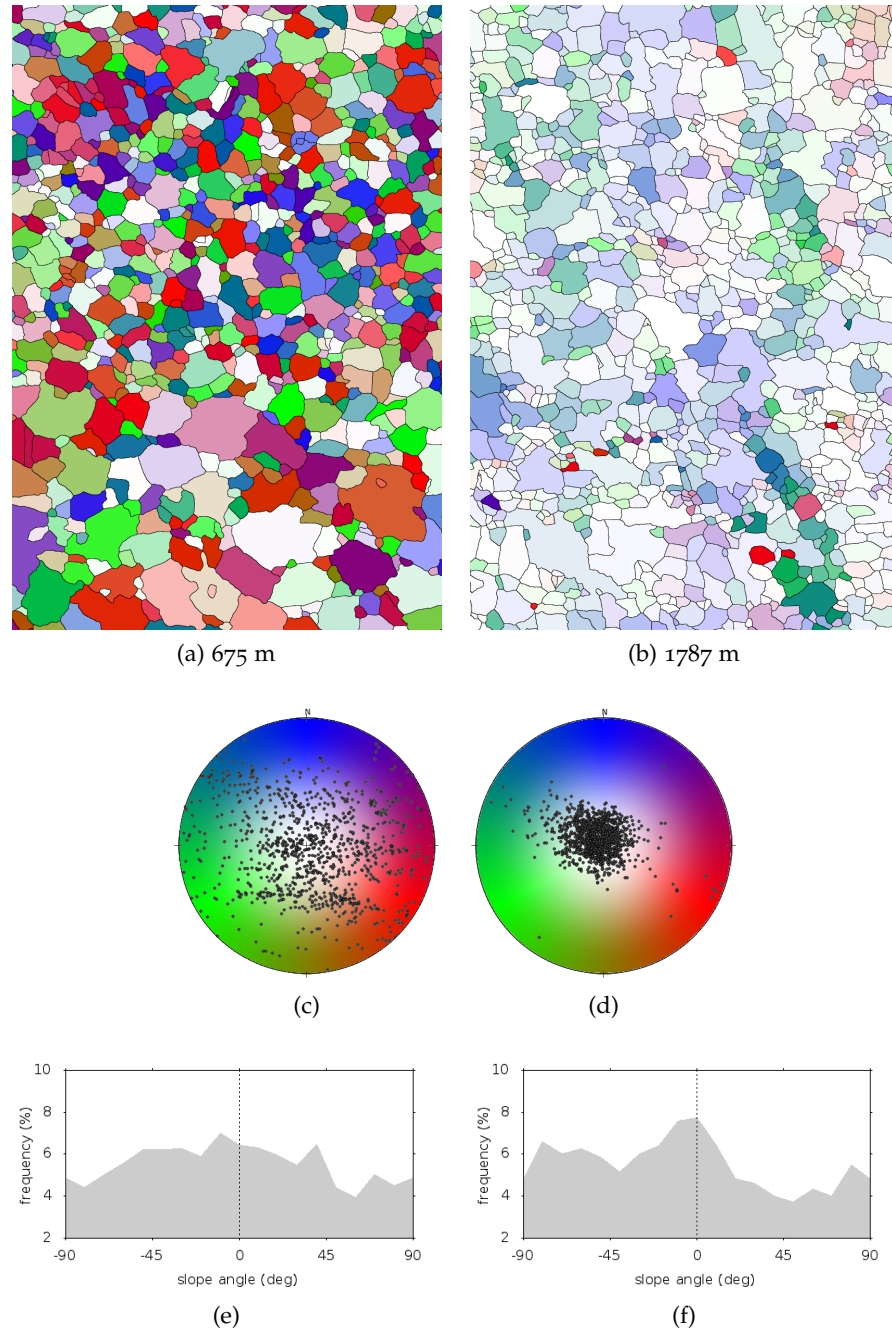


Figure 29: Detected grain boundaries in two samples from different depths: (a) Holocene ice from 675 m and (b) Ice Age ice from 1787 m. The average grain c-axes are plotted in the Schmidt diagrams (c), (d). Grain boundary slope angle distributions were calculated and plotted in (e), (f).

there is a clear tendency of the GBs to be oriented either horizontally or vertically in the image reference frame (slope angle distribution maxima at $\beta \approx 0^\circ, \pm 90^\circ$). A minimal part of boundaries is oriented in the diagonal directions ($\pm 45^\circ$). This pattern is typical for depths with a strong *c*-axes single maximum (1400-2200 m) and in pronounced cases is visible to the naked eye in the images. The correlation of the single maximum with the affinity of grain boundaries to exhibit a vertical or horizontal orientations in these depths suggests a connection between the crystallography and the GB orientation. This shall be the focus of the next two subsections.

5.4.1 Low Angle Boundaries: N-Type vs. P-Type

Section 5.3 demonstrated that the creation of new low-angle boundaries due to rotation recrystallization takes place virtually in all depths along the NEEM ice core, which is in accordance with findings for an Antarctic ice core (EDML; Weikusat et al. (2009)). In this section, I shall focus on low angle boundaries studying the geometrical relationship between the grain-boundary orientation and the crystal orientations of separated grains.

Weikusat et al. (2011) studied subgrain boundaries in ice from the EDML² ice core using X-ray Laue diffraction. They found that 110 out of 165 measured subgrain boundaries were either parallel (45 boundaries) or normal (65 boundaries) to the basal plane, with the rotation axis coinciding with one of the *a*-axes of the hexagonal crystal. These two most frequent types of low-angle GBs – the *N-type* and the *P-type* – correspond to the model of a *symmetric tilt boundary* (Weertman and Weertman, 1992), which is formed by an array of edge dislocations (Figure 30). The arrangement of edge dislocations through slip in the basal plane, which is expected to be the most common one in ice (see Section 2.3) gives rise to the *N-type* boundary. On the other hand, the *P-type* is formed by non-basal dislocation glide in a non-basal plane.

The goal of this section is to classify the grain boundaries obtained through the image segmentation in terms of their similarity to one of these two types. The difference between Laue diffraction and polarized light microscopy is that the Laue method determines the full crystal orientation, including the *a*-axes. This allows further detailed characterization of the *P-type* subgrain boundaries where no misorientation of *c*-axes occurs (see Weikusat et al. (2011)). The main problem for both methods, however, is that they cannot provide the full orientation of the GB interface. The normal vector of the plane $\mathbf{n} = (n_x, n_y, n_z)$ is projected into the image plane losing in this way its third dimension $\mathbf{n}' = (n_x, n_y, 0)$. In other words, the GB is represented through a line instead of a plane. Hence, there is no way of reconstructing the full boundary orientation from the image. This

² EPICA Dronning Maud Land

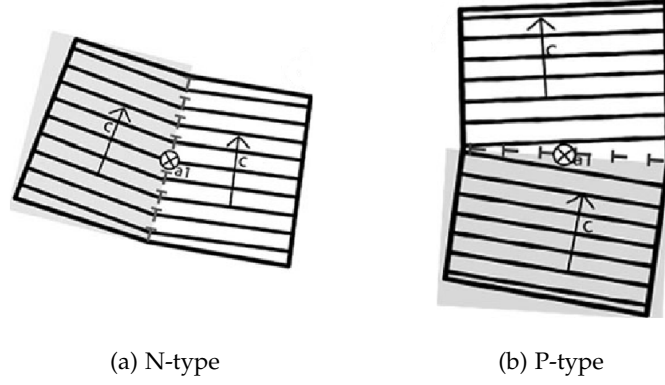


Figure 30: (a) N-type and (b) P-type grain boundary taken from Weikusat et al. (2011). The parallel lines represent the basal planes, the arrows are the c-axis vectors. The rotation vectors point into the image plane.

radical limitation inhibits the direct comparison of the GB plane with the basal planes given through the c-axes. Thus, the method presented here should be rather seen as a qualitative study. It compares the measured GB-trace orientation with the projection of a corresponding N-type boundary obtained from the crystal orientations of the adjacent grains.

5.4.2 Deviation from the Symmetric Tilt Boundary

The normal vector of a basal tilt boundary is perpendicular to the rotation vector \mathbf{r} (Figure 31). In the symmetric case the angles between the grain-boundary plane and the c-axes of the adjacent grains are equal. Thus the normal of the ideal symmetric tilt boundary is given through:

$$\begin{aligned}\mathbf{n}_t &= (\mathbf{c}_1 + \mathbf{c}_2) \times \mathbf{r} \\ &= (\mathbf{c}_1 + \mathbf{c}_2) \times (\mathbf{c}_1 \times \mathbf{c}_2) .\end{aligned}\quad (29)$$

The projection of the normal onto the image plane \mathbf{n}'_t defines the normal of the boundary trace which would be measured if the GB in the image would be a symmetric tilt boundary. Thus, the *deviation from the symmetric basal tilt boundary*

$$\omega_t = \arccos |\mathbf{n}' \cdot \mathbf{n}'_t| .\quad (30)$$

is considered. ω_t measures the angle between the theoretical tilt boundary trace in the image plane and the actually measured GB line (\mathbf{n}'). $\omega_t = 0^\circ$ indicates a perfect match of the two orientations and $\omega_t = 90^\circ$ stands for the measured grain-boundary trace lying perpendicular to the theoretical one.

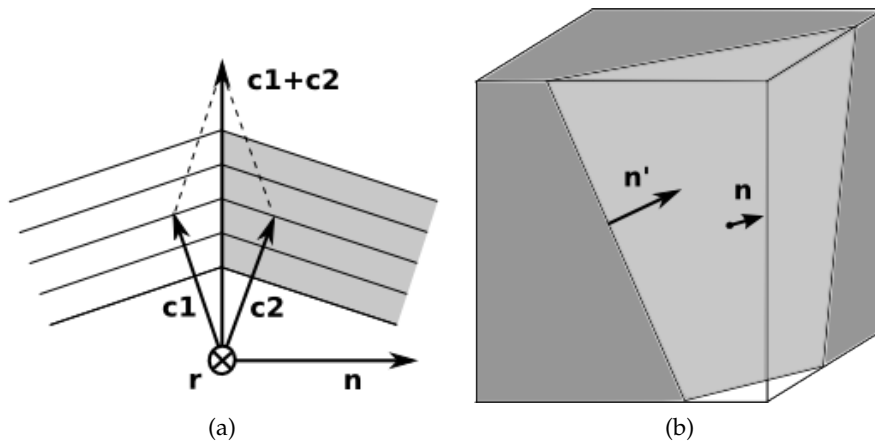


Figure 31: (a) Symmetric basal tilt boundary with the two c-axis vectors c_1 and c_2 of the adjacent grains, the rotation vector r , and the normal vector n . (b) The projection of the normal vector n' into the image plane (the front face of the cube).

Figure 32a shows the distribution of ω_t for straight boundaries with the misorientation angle between the adjacent grains $\gamma \leq 10^\circ$. The histogram indicates a rather surprising direct evidence for the GB-orientation dependence on the crystallography of the adjacent grains. Although all possible deviation angles are present, there is a continuing maximum of small ω_t . Between 600 m and 1400 m around 20% of the present boundaries exhibit a deviation from the symmetric basal tilt boundary ω_t less than 10° . This suggests a continuing formation of new grain boundaries along the whole ice core depth by "classical polygonization" via almost ideal symmetric tilt boundaries with basal dislocations.

Between 1400 m and 2200 m – i.e. in the Glacial ice – a relatively high cumulation of grain boundaries perpendicular to the orientation of the basal tilt boundary ($\omega_t \rightarrow 90^\circ$) can be observed. At first glance this seems to be an indication for the formation of the *P-type* boundaries. However, remember that ω_t compares the orientations of lines in the image and not the true planes. Thus, a right angle ω_t does not necessarily indicate orthogonality of the planes. Figure 33 shows two orthogonal planes viewed from two different points. Depending on the direction of observation, the boundary lines in a fabric image would appear to enclose different angles. The high frequency of boundaries with ω_t approaching 90° is therefore not a proof for the formation of the *P-type* boundaries. Thoroughly, it only demonstrates the generation of grain boundaries whose trace in the image plane is perpendicular to the orientation of the basal tilt boundary. Nevertheless, the onset of the high deviation maximum in 1400 m depth (Figure 32a) could be interpreted as an increased occurrence of non-basal dislocations as GB-forming dislocations, possibly because stresses in this regime reach a certain threshold due to the overload pressure.

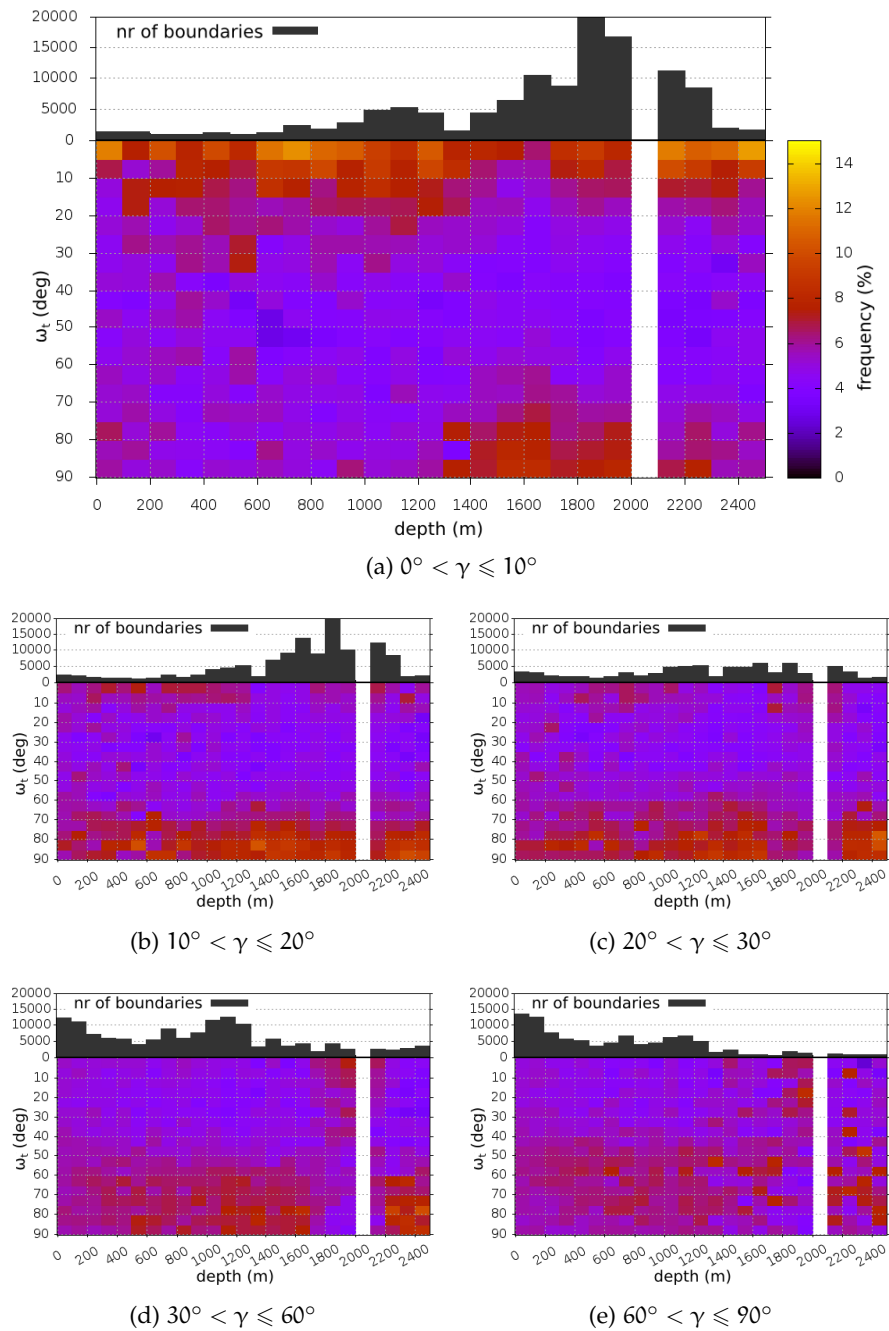


Figure 32: Deviation ω_t from the symmetric basal tilt boundary as a function of depth. The distribution changes with increasing intergranular misorientations γ .

However, the coincidence with the Holocene-Glacial transition and the sudden appearance of the maximum with depth suggest more complicated mechanisms which also include impurity influence.

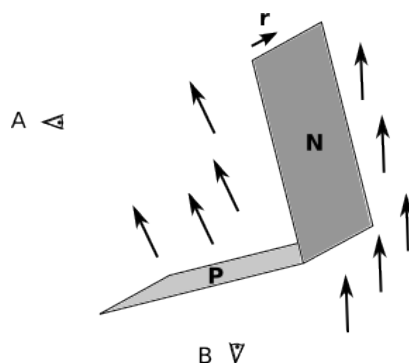


Figure 33: N-type and P-type grain boundary seen from two different points A and B. The longer arrows symbolize the c-axes vectors, the shorter arrow is the rotation vector r . For an observer at B, the boundary lines in a fabric image would appear at right angle to each other. An observer at A would see two parallel horizontal lines.

The distribution of ω_t changes significantly with increasing grain misorientation γ . Figure 32 compares the distributions for different ranges of the misorientation angle. At $10^\circ < \gamma \leq 20^\circ$ the high population of *N-type* boundaries disappears. In exchange, the orthogonal-type boundaries (ω_t close to 90°) appear with a relatively higher frequency along the whole ice core length. This distribution remains also at higher misorientations γ . The maximal occurrence stays for boundaries with ω_t close to 90° and the width of the maximum dissolves with increasing misorientation γ .

In summary, the orientations of the detected grain boundaries exhibit the following trend: GBs with orientations close to the geometry of the basal-symmetric-tilt boundary are more frequent at the lowest misorientations ($\gamma \leq 10^\circ$). Contrary to this, boundaries orthogonal to this orientation (possibly formed by non-basal dislocations) are more frequent at misorientation angles higher than 10° . The question is what processes are responsible for this asymmetric behavior of the two types of low-angle boundaries? One possible interpretation is that the basal tilt boundaries obtain a higher mobility with increasing misorientation angle. In this case, they would change their orientations and their shapes due to basal slip more likely than the orthogonal-type boundaries. This assumption, however, is purely hypothetical and cannot be supported by solid data at present.

SUMMARY AND OUTLOOK

This Diploma thesis consists of the development and application of a computer program for an automatic analysis of high-resolution c-axes images based on Digital Image Processing (DIP) routines. The code is written in C++ making use of the `VIGRA` library and the `CGP` package (see [Equation A](#)). In order to detect grains and grain boundaries, the program uses a segmentation algorithm adapted to the metric of a fabric image, where pixels represent orientations of unit vectors in space. For both objects – the grains and grain boundaries – a set of geometric parameters describing their shape and orientation is extracted.

The method developed here is applied to an extensive set of fabric data recorded along the [NEEM](#) ice core ([Chapter 5](#)). C-axes orientation distributions along the ice core length is studied using the second order orientation tensor. A sharp increase in the c-axes alignment is found in the middle part of the ice core (1400-1500 m), which is correlated with the transition between the Holocene and the Glacial period. This feature suggests a change in the flow regime induced by a combination of a different viscosity of Ice Age ice and a higher impact of the shear component of stress. The study of adjacent grain misorientation distributions demonstrates a higher cumulation of low misorientation boundaries than expected due to Monte-Carlo-simulated grain pairs. This is evidence of the ongoing creation of new grain boundaries by polygonization along the whole ice core length. Further, the geometry of grain boundaries is studied. The variability of grain-boundary straightness suggests migration recrystallization being active in the brittle zone and in the Eemian ice. Orientations of grain boundaries are studied in the ice-core reference frame as well as relatively to the crystallography of the adjacent grains. Grain boundaries exhibit preferred orientations orthogonal or parallel to the basal plane. This corresponds to the formation of new grain boundaries by dislocation glide in the basal plane as well as by non-basal dislocation arrangement in non-basal planes.

The presented results should be seen as an example of possible applications of computer-vision-based techniques to the analysis of ice c-axes. The potential of the method is by far not exhausted by this thesis, which might be a motivation for future work.

A possible improvement in order to optimize the performance of the program and the segmentation results could be an implementation of an automatic detection of image artifacts such as sample fractures and microtome scratches ([Section 4.3.3](#)). Furthermore, new ap-

proaches such as the analysis of c-axes orientation variability within individual grains and the detection of subgrain boundaries could be integrated. Intragranular lattice misorientations could be a direct link to the amount of strain energy stored within single grains. The study of crystal orientation variability along a grain boundary in combination with the boundary geometry would lead to a better understanding of dynamic recrystallization. First steps in this direction have been taken by Eric Gleiß during his internship at AWI in summer 2012 using the code developed for this thesis (Figure 34). However, the detection of fine intragranular structures worked only in particular cases so far. The main limiting factors are the relatively high signal noise and the artificial orientation gradient produced by the FA device (Section 4.1.2).

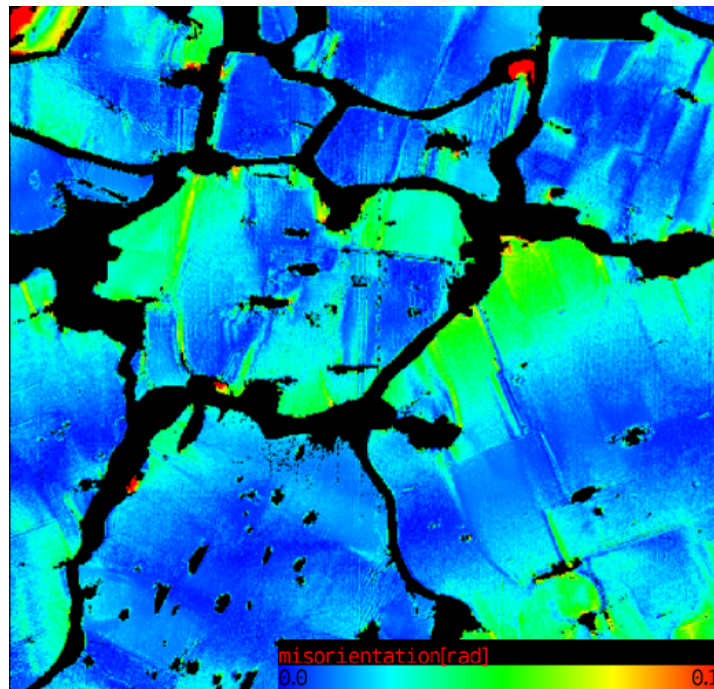


Figure 34: Intragranular structures, image by Eric Gleiß using the *cAxes* program. Misorientations between each pixel and the averaged grain c-axis are visualized by the color-code.

A collaborate software project was initiated with the aim to combine the presented method with the analysis package for LASM records developed by Tobias Binder (Binder et al., 2013). The overall goal is to establish an analytical method that combines the advantages of both microscopic techniques – the more precise grain boundary network obtained by the LASM and the c-axis orientations measured by polarized-light microscopy.

APPENDIX

MISORIENTATION-PDF OF THE UNIFORM C-AXES DISTRIBUTION

The Probability Density Function (PDF) $p(\varphi, \theta)$ of a uniform c-axes orientation distribution is the surface of a half sphere with the surface area equal to one,

$$dp(\varphi, \theta) = \frac{1}{2\pi} \sin \theta \, d\theta \, d\varphi. \quad (31)$$

Considering two random c-axes vectors we can choose the coordinate system in such a way that one of the vectors points in the z-direction. In this reference frame the misorientation angle γ between the two vectors is equal to the inclination angle θ' of the second vector. The PDF of θ' is obtained by integration over all possible azimuth values,

$$\begin{aligned} dp(\theta') &= \frac{1}{2\pi} \sin \theta' \, d\theta' \int_0^{2\pi} d\varphi' \\ &= \sin \theta' \, d\theta'. \end{aligned} \quad (32)$$

This is equal to the PDF of the misorientation angle γ between two random grains, as described in [Equation 28, Section 5.3](#).

SOFTWARE AND LIBRARIES USED

- The `VIGRA` Computer Vision Library for Generic Programming developed by Dr. Ullrich Köthe, Heidelberg Collaboratory for Image Processing (HCI), University of Heidelberg.
<http://hci.iwr.uni-heidelberg.de/vigra/>
- `CGP`: A free `C++/MATLAB` package for extracting the geometry and topology from very large volume segmentations. Developed by Bjoern Andres and Thorben Kroeger, HCI, University of Heidelberg.
<http://hci.iwr.uni-heidelberg.de/MIP/Software/cgp.php>
- `OpenStereo`: An Open Source, cross-platform software for structural geology analysis. This software was used for the creation of Schmidt diagrams.
<http://www.igc.usp.br/index.php?id=391>
- The data plots were created using `Gnuplot`, a command-line driven graphing utility.
<http://www.gnuplot.info/>
- `Inkscape`: An Open Source vector graphics editor.
<http://inkscape.org/>
- This document was typeset using the typographical look-and-feel `classicthesis` developed by André Miede. The style was inspired by Robert Bringhurst's seminal book on typography "*The Elements of Typographic Style*". `classicthesis` is available for both \LaTeX and `LyX`:
<http://code.google.com/p/classicthesis/>

The work related to this thesis has been done using mainly software under the GNU General Public License or other free software.

BIBLIOGRAPHY

- J. F. Adam. Methoden und Algorithmen zur Verwaltung und Analyse axialer 3-D-Richtungsdaten und ihrer Belegungsdichten. *Goettinger Arb. Geol. Palaontol.*, 40:100, 1989. Z 1317 - 40 1989.
- R.B. Alley, A.J. Gow, and D.A. Meese. Mapping c-axis fabrics to study physical processes in ice. *J. Glaciol.*, 41(137):197–203, 1995.
- N. Azuma and A. Higashi. Formation processes of ice fabric pattern in ice sheets. *Ann. Glaciol.*, 6:130–134, 1985.
- T. Binder, C.S. Garbe, D. Wagenbach, J. Freitag, and S. Kipfstuhl. Extraction and parameterization of grain boundary networks, using a dedicated method of automatic image analysis. *Journal of Microscopy*, 250:130–141, 2013. doi: 10.1111/jmi.12029.
- J. A. Church, J. M. Gregory, P. Huybrechts, M. Kuhn, K. Lambeck, M. T. Nhuan, D. Qin, and P. L. Woodworth. Change in Sea Level. In J. T. Houghton, Y. Ding, D. J. Griggs, M. Noguer, P. J. Van der Linden, X. Dai, K. Maskell, and C. A. Johnson, editors, *Climate Change 2001: The Scientific Basis. Contribution of Working Group I to the Third Assessment Report of the Intergovernmental Panel on Climate Change*, pages 639–693. Cambridge University Press, Cambridge, United Kingdom and New York, NY, USA, 2001.
- M. R. Drury and J. L. Urai. Deformation-related recrystallization processes. *Tectonophysics*, 172:235–253, 1990.
- G. Durand, O. Gagliardini, Th. Thorsteinsson, A. Svensson, S. Kipfstuhl, and D. Dahl-Jensen. Ice microstructure and fabric: an up-to-date approach for measuring textures. *J. Glaciol.*, 52(179):619–630, December 2006. doi: 10.3189/172756506781828377.
- G. Durand, A. Persson, D. Samyn, and A. Svensson. Relation between neighbouring grains in the upper part of the NorthGRIP ice core - Implications for rotation recrystallization. *Earth Planet. Sci. Lett.*, 265:666–671, 2008.
- O. Gagliardini, G. Durand, and Wang. Y. Grain area as a statistical weight for polycrystal constituents. *J. Glaciol.*, 2004.
- J. W. Glen. The creep of polycrystalline ice. *Proc. Roy. Soc. London*, A228:519–538, 1955.
- G. Gottstein and L. S. Shvindlerman. *Grain boundary migration in metals*. CRC Press, 1999.

- P. V. Hobbs. *Ice Physics*. Oxford University Press, 1974.
- T. H. Jacka and L. Jun. Flow rates and crystal orientation fabrics in compression of polycrystalline ice at low temperatures and stresses. In T. Hondoh, editor, *Physics of Ice Core Records*, pages 83–102. Hokkaido University Press, Sapporo, 2000. URL <http://eprints.lib.hokudai.ac.jp/dspace/handle/2115/32487>.
- NEEM community members. Eemian interglacial reconstructed from a Greenland folded ice cores. *Nature*, 493:489–494, 2013. doi: 10.1038/nature11789. URL <http://www.nature.com/nature/journal/v493/n7433/full/nature11789.html>.
- NEEM website, April 2013. URL <http://neem.dk/>.
- W. S. B. Paterson. *The physics of glaciers*. Butterworth-Heinemann, Elsevier, third edition, 1994. ISBN 0-7506-4742-6.
- V. F. Petrenko and R. W. Whitworth. *Physics of ice*. Oxford University Press, 1999. ISBN 0-19-851894-3.
- F. Riche, M. Montagnat, and M. Schneebeli. Evolution of crystal orientation in snow during temperature gradient metamorphism. *Journal of Glaciology*, 59(213):47–55, 2013.
- A.E Scheidegger. On the statistics of the orientation of bending planes, grain axes, and similar sedimentological data. *U.S. Geological Survey Professional Paper*, 525-C, 1965.
- J. Surma. Die Orientierungen der C-Achsen im NEEM Eiskern (Grönland). Master's thesis, Institut für Geologie und Mineralogie, Universität zu Köln, 2011. Bachelor of Science Geowissenschaften.
- S. Suzuki. Grain Coarsening of Microcrystals of Ice. (III). *Low Temperature Science Ser. A*, 28:47–61, 1970.
- A. Tammen. Mikrostruktur im Eis - Hochaufgelöste Korngrößen- und c-Achsenanalyse im NEEM-Kern (Grönland). BSc-thesis, Institut für Geowissenschaften an der Johannes Gutenberg-Universität Mainz *Alfred Wegener Institut für Polar- und Meeresforschung Bremerhaven, November 2012. URL <http://epic.awi.de/32299/>.
- L. Vincent and P. Soille. Watersheds in digital spaces: an efficient algorithm based on immersion simulations. *Pattern Analysis and Machine Intelligence, IEEE Transactions on*, 13(6):583–598, 1991. ISSN 0162-8828. doi: 10.1109/34.87344.
- E. Wallbrecher. *Tektonische und gefügeanalytische Arbeitsweisen*. Ferdinand Enke Verlag Stuttgart, 1986. geo 326 19.

- Y. Wang. *The development of an automatic analyzer for fabrics and textures of polar ice cores*. PhD thesis, Nagaoka University of Technology, 1999.
- Y. Wang, Th. Thorsteinsson, S. Kipfstuhl, H. Miller, D. Dahl-Jensen, and H. Shoji. A vertical girdle fabric in the NorthGRIP deep ice core, North Greenland. *Ann. Glaciol.*, 35:515–520, 2002.
- J. Weertman and J. R. Weertman. *Elementary Dislocation Theory*. Oxford University Press, 1992.
- I. Weikusat, S. Kipfstuhl, S. H. Faria, N. Azuma, and A. Miyamoto. Subgrain boundaries and related microstructural features in EPICA-Dronning Maud Land (EDML) deep ice core. *J. Glaciol.*, 55(191):461–472, 2009. doi: 10.3189/002214309788816614.
- I. Weikusat, A. Miyamoto, S. H. Faria, S. Kipfstuhl, N. Azuma, and T. Hondoh. Subgrain boundaries in Antarctic ice quantified by X-ray Laue diffraction. *J. Glaciol.*, 57(201):85–94, 2011. doi: 10013/epic.36402.
- J. Wheeler, D. J. Prior, Z. Jiang, R. Spiess, and P. W. Trimby. The petrological significance of misorientations between grains. *Contributions to Mineralogy and Petrology*, 141:109–124, 2001.
- C. J. L. Wilson, D. S. Russell-Head, and H. M. Sim. The application of an automated fabric analyzer system to the textural evolution of folded ice layers in shear zones. *Ann. Glaciol.*, 37:7–17, 2003.
- N. H. Woodcock. Specification of fabric shapes using an eigenvalue method. *Geological Society of America Bulletin*, 88(9):1231–1236, September 1977. doi: 10.1130/0016-7606(1977)88<1231:SOF SUA>2.o.CO;2. URL <http://gsabulletin.gsapubs.org/content/88/9/1231.abstract>.

ACKNOWLEDGMENTS

I want to express my sincere gratitude to my supervisor Dr. Ilka Weikusat for her expertise guidance, generous support and patience. She offered me a fascinating topic and provided me excellent facilities and maximal liberty for a creative work.

I owe my deep gratitude to Prof. Dr. Dr. Günter Kaindl for his active support and constructive suggestions during the whole time of my work on this thesis.

I would like to appreciate Dr. Sepp Kipfstuhl for his valuable suggestions. His consultations helped me to see concrete problems in a wider context.

Many thanks to Tobias Binder for his kind support in all questions related to programming, hardware and image analysis, as well as for providing me his source code.

I am very thankful to S. Kipfstuhl, M. Montagnat, A. Svensson, D. Samyn, S. Sato and I. Weikusat for sample measurements and providing the data.

Many thanks to all colleagues and members of the department of Glaciology at the [AWI](#) for creating a familiar and motivating ambience.

Very special thanks to my family and my nearests for their support, inspiration and love.

DECLARATION

I hereby affirm that this thesis is my own original work and that no other sources and utilities were used besides those declared in the text.

Ich versichere hiermit, dass ich diese Arbeit selbständig verfasst und keine anderen als die im Text angegebenen Quellen und Hilfsmittel benutzt habe.

Berlin, 29. April 2013

Jan Eichler